Theoretical and Experimental Analyses of Liquid Transport in Fluidic Systems with Micro/Nanostructured Surfaces: Toward Applications in Separation Processes

A Dissertation Presented

by

Dhiraj Nandyala

to

The Graduate School

in Partial Fulfillment of the

Requirements

for the Degree of

Doctor of Philosophy

in

Mechanical Engineering

Stony Brook University

May 2021

Stony Brook University

The Graduate School

Dhiraj Nandyala

We, the dissertation committee for the above candidate for the

Doctor of Philosophy degree, hereby recommend

acceptance of this dissertation.

Dr. Carlos E. Colosqui - Dissertation Advisor
Associate Professor, Mechanical Engineering Department

Dr. Thomas Cubaud - Chairperson of Defense
Associate Professor, Mechanical Engineering Department

Dr. David Hwang - Committee Member
Associate Professor, Mechanical Engineering Department

Dr. Andrei Fluerasu - Co-advisor and Outside Member
Lead Beamline Scientist, Brookhaven National Laboratory

This dissertation is accepted by the Graduate School

Eric Wertheimer

Dean of the Graduate School

Abstract of the Dissertation

Theoretical and Experimental Analyses of Liquid Transport in Fluidic Systems with Micro/Nanostructured Surfaces: Toward Applications in Separation Processes

by

Dhiraj Nandyala

Doctor of Philosophy

in

Mechanical Engineering

Stony Brook University

2021

This doctoral dissertation involves the theoretical and experimental analyses of liquid transport in fluidic devices that have surfaces with either natural or synthetic micro/nanoscale structures that significantly affect interfacial processes such as wetting and spreading, imbibition and drainage, and liquid transport driven by pressure and/or capillary forces. The first research project of this dissertation involves research work performed at the National Synchrotron Light Source (NSLS-II) of Brookhaven National Laboratory (BNL) where the X-ray Photon Correlation Spectroscopy (XPCS) techniques have been employed to characterize flow velocity profiles and rheological properties of colloidal fluids. A Fourier decomposition technique and a multivariable optimization algorithm were developed and applied to determine the flow velocity profiles and mass diffusivity from the intensity autocorrelation function obtained from the XPCS experiments. The second research project of this dissertation involves the design, fabrication, and characterization of a fluidic diode device for potential application in water-oil separation and microfluidic handling. Theoretical and experimental results indicate that a simple capillary device with micro/nanopatterned glass surfaces can be employed as a fluidic diode due to the presence of a large surface energy barrier preventing the transport of specific fluid pairs. The scientific and technical knowledge gained from the projects performed for this doctoral dissertation can have a significant impact on the design of novel micro/nanofluidic devices for passive separation, detection, and actuation.

Dedication Page

To my parents, Lalitha and Madhusudhana Rao Nandyala and my cousins/siblings, for all their support.

Contents

List of Figures

List of Tables

Chapter 1

Introduction

1.1 Overview

This doctoral dissertation work deals with the theoretical and experimental analysis of liquid transport in fluidic channels, small capillaries, or pores that have surfaces with either natural or synthetic structures that significantly affect the dynamics of interfacial processes such as wetting and spreading, imbibition and drainage, or liquid flow driven by pressure and/or capillary forces. These phenomena produce macroscopic effects that are highly sensitive to the nanoscale structure of the liquid-solid interfaces involved and it is therefore multiscale in nature and can be difficult to predict and control. A better understanding of these complex interfacial processes through the development of analytical models and the experimental verification of their predictions will help the research community to develop new applications for the separation of immiscible liquids, different phases of colloidal systems, and/or molecular and particulate solutes in micro- or nanofluidic devices, among many others. To achieve such a better understanding, diverse micro/nanoscale fabrication and experimental characterization techniques have been employed in this dissertation work, in combination with numerical algorithms for analyzing and interpreting large volumes of data, and theoretical model developments based on classical continuum-based descriptions.

This dissertation work comprises two main projects described in Chapters 3 and 4 of this doctoral dissertation: (1) Development of a new experimental analysis method by which spectroscopy techniques such as synchrotron-based X-ray Photo-electron Correlation Spectroscopy (XPCS) can be employed for the characterization of fluid flows and transport of solutes (e.g., nanoparticles, macromolecules) in capillary channels or pores. The development of the analysis method and experimental study performed is described in Chapter 3.

(2) Design and characterization of capillary diode-like devices with surfaces having both a microscale pattern and nanoscale surface features, that can be applied for the separation of immiscible liquids, such as water and oils, and other technical applications involving selective liquid transport through capillary conducts. The analytical modeling and experimental characterization of the studied capillary diodes is presented in Chapter 4.

To conclude this doctoral dissertation, Chapter 5 presents a summary of the main findings, and outlines potential future work that could build upon these findings to address open questions and technical challenges.

1.2 Fluid Flow Analysis via X-ray Photon Correlation Spectroscopy

Different X-ray scattering techniques have been used over the past several years to probe the dynamics of colloids and soft matter [3–5]. In particular, the X-ray Photon Correlation Spectroscopy (XPCS) technique has been extensively used for flowing samples owing to the advantages it has over other scattering techniques such as Dynamic Light Scattering [3,6]. The XPCS and other correlation spectroscopy techniques are based on extracting physical information from the intensity autocorrelation function, which is obtained from temporal fluctuations of the speckle pattern produced by x-ray scattering on a highly sensitive photon detector. Employing tracer nanoparticles (30-100 nm) in the studied fluid or colloidal system, it is thus possible to determine flow characteristics such as the velocity flow profile from the intensity autocorrelation function produced by scattering of the incoming x-ray beam by the tracers at various spatial positions. In similar way, one can determine the diffusivity of tracer nanoparticles and from there the local viscosity of the liquid using the Stokes-Einstein relation, as done in microrheology studies with conventional optical techniques [7].

Previous XPCS studies for laminar flow inside a cylindrical capillary assumed a classical parabolic flow profile and no-slip boundary conditions to determine analytically the autocorrelation function [3]. The analytical autocorrelation function derived by assuming unbiased Brownian motion and Poiseuille flow reported good agreement with experimental results [3,8] which confirms the model assumptions with a short-time scale dissipative dynamics due to Brownian motion and longer decay time associated with the shear response due to bulk motion using the intensity autocorrelation functions.

The work in this doctoral dissertation develops and demonstrates a “model-free” reconstruction for the flow profiles by decomposing flows into discrete sets of Fourier modes and finding the set of modes that minimize a measure of the error between the computed guess and the experimentally determined autocorrelation function. In this dissertation, I will discuss the criteria for the selection of the “optimal” Fourier modes and show by reducing the mean-square-error between the computed and experimental autocorrelation one can recover the classical parabolic flow profile for Newtonian fluid flow. The best set of Fourier modes is determined by an iterative process and conventional strategies for minimization of the mean-square-error. The developed method in this study can give valuable insights into the dynamics of complex colloidal liquids when there is no a priori information available about its rheological properties and thus the flow profile in a cylindrical capillary channel cannot be assumed as parabolic.

1.3 The XPCS technique

Various techniques such as DLS also known as Photon Correlation Spectroscopy (PCS) were performed in the past to study dynamics of complex colloidal fluids in disordered systems [9,10]. However XPCS provides an advantage that it does not have the problem of multiple scattering and it can be used to probe dynamics of systems at higher momentum transfer [1, 11]. The comparison between XPCS and other techniques are shown in Fig **1.1**.

When a disordered condensed matter system such as complex colloidal suspensions is exposed to coherent X-ray beam, it generates a speckle pattern. The resulting instantaneous intensity is given by square of total field $\mathbf{E}(\mathbf{q},t)$ [6].

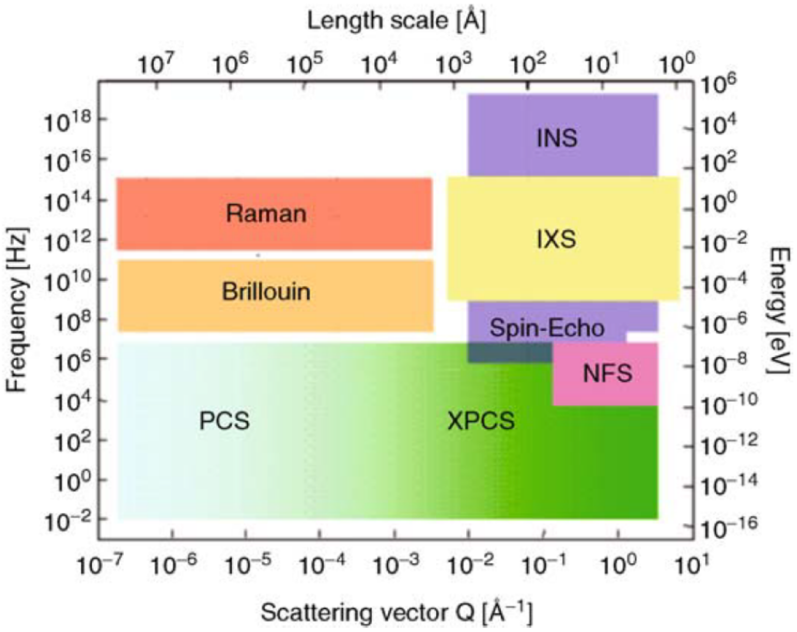

Figure 1.1: Frequency-Scattering vector space covered by X-ray Photon Correlation Spectroscopy (XPCS) and complementary techniques (PCS-Photon Correlation Spectroscopy, INS-Inelastic Neutron Scattering, IXS-Inelastic X-ray Scattering, NFS-Nuclear Forward Scattering) [1]

$$I(\mathbf{q},t) = |\mathbf{E}(\mathbf{q},t)|^2 = \left|\sum_n b_n(\mathbf{q}).e^{i\mathbf{q}.\mathbf{r}_n(t)}\right|^2 \tag{1.1}$$

where $b_n(\mathbf{q})$ is the scattering amplitude of the n^{th} scatterer located at position $\mathbf{r}_n(t)$, $\mathbf{q}$ is the scattering wave vector.

As the studied system fluctuates with time, the speckle pattern also changes. Therefore, information about the dynamics of the system can be obtained by measuring temporal fluctuations of the speckle pattern. This can be quantified via second order intensity fluctuation autocorrelation functions $g^{(2)}(\mathbf{q},t)$.

1.4 Wetting and interfacial phenomena on micro- and nanopatterned surfaces

In Chapter 4 of this dissertation, I discuss results for a simple capillary device that employs micro-patterned surfaces to promote or prevent selectively the adsorption of water and oils. The micropattern produces a difference in surface energies and an effective energy barrier that results in diode-like behavior for the capillary conduction of water.

Well-established thermodynamic arguments and extensive experimental studies indicate that the wetting behavior of different liquids can be controlled by designing the micro- or nanoscale structure or roughness of a solid surface [12–17] In some cases the micro- or nanoscale structure or roughness of a surface can significantly increase the interfacial area with direct contact with a wetting fluid and effectively increase the surface energy per projected unit area, as described by the Wenzel equation [18]. In other cases, depending on the affinity between the wetting fluids and the solid phase, the surface structure or roughness can entrap small domains of one fluid phase producing a heterogeneous surface with a dramatically different effective surface energy, as predicted by the Cassie-Baxter model [19]. Furthermore, multiple local minima in the system energy and thus metastable equilibrium states can be induced by the micro/nanostructure of a surface, which has been found to substantially hinder or even prevent wetting processes such as spontaneous or forced spreading, capillary imbibition, or interfacial adsorption [20–25]. Engineering the micro/nanostructure of a surface can thus provide pathways to control the static and dynamic wetting behavior of different liquids such as water and oil.

In the case of wetting by water in ambient air, proper combinations of surface chemistry and physical structure produce macroscopically observed superhydrophobic [26–28] or superhydrophilic [29–32] behaviors that are characterized by extremely high ($\gtrsim 150^\circ$) or low ($\lesssim 10^\circ$) apparent contact angles, respectively. The contact angle hysteresis can become negligibly small for certain combinations of surface micro/nanostructure and geometric configurations (e.g., sessile droplet, static meniscus), which leads to very small liquid adhesion forces and the associated self-cleaning and antifouling effects [27, 33, 34]. Analogous wetting phenomena can be observed for the case of oils wetting a solid, in which case micro/nanostructured surfaces can display superoleophobic or superoleophilic properties [35–38]. However, the fabrication of surfaces with robust and stable omniphobic properties that prevent adhesion of different liquids and oils presents significant challenges that cannot be easily overcome due to surface contamination and chemical transformations over long times with associated undesirable effects.

Efforts to overcome these challenges led to the development of liquid-infused surfaces (LISs) with the micro- or nanoscale structure of the surface filled with liquid having high affinity to the surface material [39–42]. Under proper conditions, the liquid filling the micro/nanostructure can form a thin stable film preventing direct contact between the wetting liquid and effectively providing a lubrication effect that significantly reduces contact angle hysteresis and adhesion forces. The macroscopic wetting behavior of a LIS is thus effectively controlled by the affinity between the infused liquid and the wetting fluid phases, which can result in a large variety of wetting configurations [43–45]. While the wetting properties of LISs have been widely studied for the case of open-surface configurations (e.g., droplet spreading on a single surface),a smaller number of studies have focused on the case of full confinement (e.g., two-phase flow in microchannels) where the coupling between pressure, gravitational, and capillary forces can give rise to diverse and complex wetting dynamics [46–49].

The work described in Chapter 4 includes the design, fabrication, and characterization of a slit microchannel with a section of prescribed length occupied by a LIS and a second section with a conventional (non-patterned) surface. Under proper conditions, a large surface energy barrier is induced at the junction between the channel section with the LIS and the conventional surface, which effectively results in a finite threshold pressure for driving net liquid flow through the channel. The energy barrier magnitude and minimum pressure head required to sustain fluid flow can be controlled by the geometric design of the slit channel and the microstructure of the LIS, and depends on the surface energy of the wetting fluids. The designed slit microchannel can be employed as a microfluidic check-valve or “capillary diode” with different threshold or cracking pressures for conducting water or oils by capillary action and pressure-driven flows in the upstream and downstream direction. In order to demonstrate the potential application of the concept for the passive separation of water and oil, we characterize experimentally the vertical capillary imbibition in the case of water or hexadecane in ambient air, and the more complex case of oil droplets and oil films spreading over a water phase. Experimental analysis reports the effective separation and selective adsorption of water by the fabricated capillary diode device under different studied conditions as described in chapter-4. Our experimental observations can be accounted for by a simple analytical model that outlines the basic principles for the design of so-called capillary diodes as potential devices for selective adsorption and separation of immiscible liquids.

Chapter 2

Theory and Background

This section describes theoretical knowledge and analytical models that are relevant to the projects performed for this doctoral dissertation. In particular, I discuss the basic equations describing capillary phenomena, wetting, and fluid flow, that are based on classical continuum descriptions that are adopted in this dissertation work in order to model the effect of the nanoscale structure of liquid-solid interfaces.

2.1 Sharp Interface Continuum thermodynamics

Continuum thermodynamics describes the necessary equilibrium conditions to study wettability of plain and heterogeneous surfaces as well as colloidal particle adsorption at interfaces. In particular, one can determine relationships between pressures and interfacial curvatures i.e Laplace pressure and the Young's contact angle for a spherical particle on a flat surface and a flat liquid-fluid interface and, droplet spreading on surfaces.

I will start by considering Gibbs's work on thermodynamics of interfaces which assumes a smooth and sharp interface between two phases. In spite of many simplifications, Gibbs' study of interfaces are widely employed to study wetting problems involving droplet spreading, wicking, adsorption at an interface. Let us begin by considering an open thermodynamic system of Volume (V) with three phases (i = 1,2,3) which are separated by a sharp surface and the corresponding interfacial areas A_{ij}. The three phase system consists of number of molecules $\mathrm{N}_{\mathrm{i}}^{(\mathrm{k})}$ of substance k which could exchange mass with a larger heat reservoir at temperature T. The chemical potential and temperature of all the phases are in equilibrium ($\mathrm{\mu_i^{(k)}} = \mu^{(k)}$ and $\mathrm{T_i = T}$). The sharp interface is assumed to be very thin, therefore does not occupy any physical volume ($\mathrm{dV} = \sum \mathrm{dV_i}$). Under these conditions, differential change in internal energy is given by

$$\mathrm{dU = TdS - \sum p_i dV_i + \sum \gamma_{ij} dA_{ij} + \mu^{(k)} dN_i^{(k)}}. \tag{2.1}$$

where γ_{ij} is the specific energy per unit area required to increase the surface area, S is the entropy of the system.

The Helmholtz free energy F at constant temperature and volume is given by $\mathrm{F = U - TS}$ and the differential change is given by

$$\mathrm{dF = -\sum p_i dV_i + \sum \gamma_{ij} dA_{ij} + \mu^{(k)} dN_i^{(k)}}. \tag{2.2}$$

where $\mathrm{dF = dU - TdS - SdT}$.

Moreover, the changes in thermodynamic system can also expressed in terms of grand potential by

$$\mathrm{d\Omega = -\sum p_i dV_i + \sum \gamma_{ij} dA_{ij}}. \tag{2.3}$$

where $\mathrm{\Omega = U - TS - \sum \mu^{(k)} dN_i^{(k)}}$ for a system evolving at constant temperature, volume and chemical potential ($\mathrm{dT = 0, dV = 0, d\mu^{(k)} = 0}$).

The Eqs. 2.1–2.3 obtained by assuming a sharp interface model with geometric simplifications gives us insights into thermodynamic global minimum. For instance, the value of contact angle obtained using this model assumes the surfaces to be ideally smooth i.e zero surface roughness. For a reader more interested in continuum thermodynamics, book by Rowlinson and Widom [50]is a good starting point. Most surfaces in nature contains surface heterogeneities and the contact angle has a diverse range of values such that $\theta_R \leq \theta_Y \leq \theta_A$, where θ_A is the advancing contact angle and θ_R is the receding contact angle of the liquid front. Consequently, the presence of surface roughness yields multiple equilibrium states governed by different wetting configurations such as the Cassie-Baxter and the Wenzel state (see Fig. 2.2). Colosqui et.al [17] goes in detail describing the wetting models for particle with nanoscale roughness and droplet dynamics on rough surfaces via Langevin dynamics and Kramer's theory for wetting using kinetic equations.

2.2 Capillary pressure

Surface Tension plays a phenomenon role in the movement of insects on water, formation of meniscus inside capillaries, emulsions, capillary bridges [51]. Let us consider liquid in a container shown in Fig. 2.1. A molecule in the bulk of liquid experiences equal cohesive forces from all the orientations but the molecules at the interface are subjected to disproportionate attractive forces from only one side. Hence there is a pressure difference between the interior part of liquid interface adjacent to the interface and atmosphere that results in a tension force, which is referred to as surface tension. This pressure difference is also the reason why the smaller droplets prefers to merge into bigger droplets.

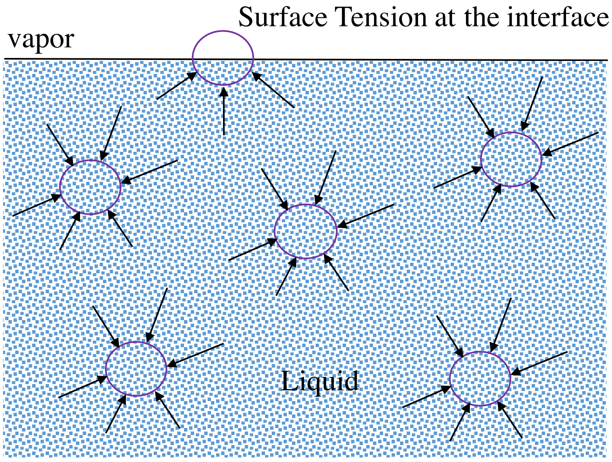

Figure 2.1: Surface Tension phenomenon showing molecular interactions in the bulk and at the interface. Net forces due to the interactions for a molecule in the bulk is zero while a molecule in interface has missing interactions from the vapor side.

Let us consider an oil droplet inside a water droplet. The work done by the pressure and capillary force to displace the oil-water interface by infinitesimal amount dR is given by [51]

$$\delta \mathrm{W} = -\mathrm{p_0 dV_0} - \mathrm{p_w dV_w} + \gamma_{\mathrm{ow}} \mathrm{dA} \tag{2.4}$$

where, $\mathrm{d}V_0$ and $\mathrm{d}V_\mathrm{w}$ are changes in the volumes of oil and water respectively, $\mathrm{p_0}$ and $\mathrm{p_w}$ are changes in the pressures of oil and water respectively and γ_{ow} is the interfacial tension between oil and water.

For equilibrium, $\delta W = 0$,

$$\delta \mathrm{P} = \frac{2\gamma_{\mathrm{ow}}}{\mathrm{R}} \tag{2.5}$$

Alternatively, we could obtain above equation by taking the derivate of grand potential (Eq. 2.3) with respect to R. Therefore, $\mathrm{d}\Omega/\mathrm{dR} = (\mathrm{p_2} - \mathrm{p_1})\mathrm{dV_1/dR} + \gamma_{12}\mathrm{dA_{12}/dR} = 0$ which gives

$$\mathrm{p}_1 - \mathrm{p}_2 = \frac{2\gamma_{12}}{\mathrm{R}}. \tag{2.6}$$

Thus from the above, we see that droplets of small size possess higher internal pressure. In more general case, Laplace's theorem states an increase in the hydrostatic pressure between the boundaries of two fluids as

$$\Delta \mathrm{p} = \gamma \left(\frac{1}{\mathrm{R}} + \frac{1}{\mathrm{R}'} \right) \tag{2.7}$$

where R and R$'$ are the radii of curvature of surface and γ is the surface tension.

2.3 Capillary rise: Jurin's law

Liquid penetration in porous solids has many applications in areas of oil lubrication, inkjet printing and self cleaning etc [52]. At a molecular level, the interaction between adhesive and cohesive forces enables capillary forces to dominate the body forces (gravity) which leads to rise in the liquid level in confinements such as cylindrical pores, capillary slits etc. This is commonly referred to as capillary rise. The reverse effect is also observed where in liquid level in a column drops when in contact with liquid, it is referred to as capillary depression. Meniscus forms an equilibrium contact angle θ_E with the inner walls of the tube. For a circular capillary, radius of the curvature in the Eq. 2.7 is given by R = R$'$ = r/cos θ_E. Hydrostatic Pressure difference Δp_g gives an estimate of the rise in liquid column h_E from the interface ($h = 0$) which is given by $\Delta p_g = \rho g h$. At equilibrium, capillary forces due to Laplace pressure balances hydrostatic pressure due to gravity (Δp = Δp_g). Hence,

$$\mathrm{h_E} = \frac{2\gamma \mathrm{cos}\theta_\mathrm{E}}{\rho \mathrm{gr}} \tag{2.8}$$

where $\mathrm{h_E}$ is the equilibrium height of liquid column, ρ is the density of liquid, r is the inner radius of capillary and g is the gravity.

The above equation is referred to as Jurin's law which describes the equilibrium height of liquid in a cylindrical cross-section to be inversely proportional to the radius of channel.

Dynamics of the liquid front is critical in understanding the imbibition and wicking of porous solids [53]. Washburn predicted the rate at which liquid rises inside a cylindrical

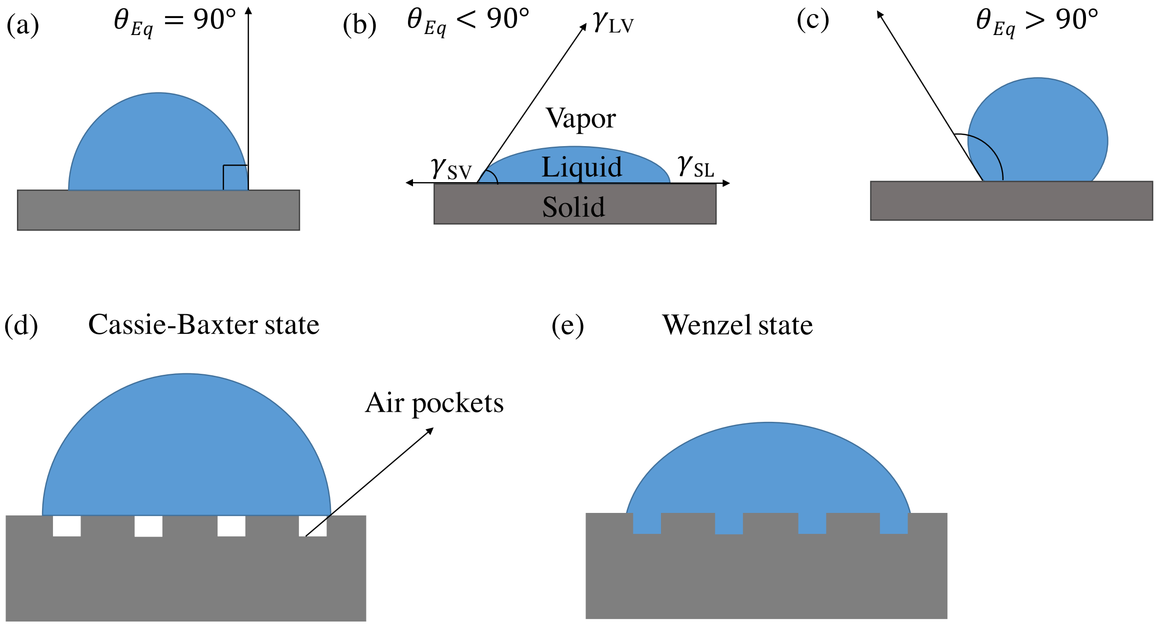

Figure 2.2: Wetting states on surfaces. (a) Neutral wetting when the equilibrium contact angle, $\theta_E = 90°$. (b) Surface is hydrophilic when $\theta_E < 90°$. (c) Surface is hydrophobic when $\theta_E > 90°$. (d) Cassie-Baxter system when a droplet sits on the top of surface asperities. (e) Wenzel system when a droplet fills the surface textures.

tubes by neglecting inertial forces and gravity. The equation describing the spontaneous liquid imbibition is referred to as Lucas-Washburn(LW) equation. It shows that the penetration length varies with square root of time as shown in Eq. 2.9

$$\mathrm{L} = \sqrt{\frac{\gamma \mathrm{rtcos}\theta_{\mathrm{E}}}{2\eta}} \tag{2.9}$$

where, L is the penetrating length or height of liquid column, γ is the surface tension of imbibing liquid, η is the dynamic viscosity of the liquid, θ_{E} is the equilibrium contact angle between solid and liquid and r is the radius of capillary.

Though L-W equation is the most used equation for describing dynamics of liquids in capillaries, it has limitations. For instance, the theory assumes that surface is smooth and homogeneous and it does not account for micro/nano scale heterogeneities which can cause significant deviations from L-W predictions [24, 47, 54].

2.4 Static contact angle and Young-Laplace equation

Wetting plays an important role in capillary imbibition and drainage of liquids. Significant research has been done in understanding wetting after discovery of the phenomenon of lotus effect [55, 56]. Specifically, contact angle plays a phenomenon role in the ability of surfaces to wet and de-wet. For instance, when a liquid droplet sits on a chemically homogeneous surface, it spreads according to the Young equation Eq. 2.10 where θ_E is the equilibrium contact angle.

$$\cos\theta_{\mathrm{E}} = \frac{\gamma_{\mathrm{SV}} - \gamma_{\mathrm{SL}}}{\gamma_{\mathrm{LV}}} \tag{2.10}$$

where , γ_{LV} is the interfacial tension between liquid and vapor, γ_{SV} is the interfacial tension between solid and vapor and γ_{SL} is the interfacial tension between solid and liquid.

In order to elucidate the wettability of a solid, a water droplet is spread on the material and the shape of droplet on the surface determines the contact angle. If the equilibrium contact angle $\theta_E < 90°$, the surface is said to be hydrophilic and if $\theta_E > 90°$, the surface is hydrophobic as shown in Fig. 2.2c. However the parameter that determines the wettability of a solid is referred to as the spreading parameter S which measures the interfacial surface energy difference and is given by

$$\mathrm{S} = \gamma_{\mathrm{SV}} - (\gamma_{\mathrm{SL}} + \gamma_{\mathrm{LV}}) \tag{2.11}$$

Hence, the liquid prefers to wet completely and forms a film if $S > 0$ in order to minimize the surface energy which is referred to as total wetting. However there exists a finite equilibrium contact angle in case of $S < 0$ as shown in Fig. 2.2b. Numerous methods have been developed over the years by many researchers to make surfaces more hydrophobic and even super-hydrophobic via morphing surfaces at the nano-scale level [26,44,57]. One of such surfaces was fabricated by our group via plasma etching of sharp nano cones on silica substrate which is super-hydrophobic with $\theta_E \simeq 150°$.

2.4.1 The Wenzel equation

Although Young's contact angle describes the relationship between interfacial energies across different states, it does not describe superwettability for homogeneous surfaces. Hence, Wenzel et.al came up with a modified Young's law by introducing an additional factor r, which is the roughness factor defined as the ratio of true surface area to the projected surface area as given by Eq. 2.12. Therefore, the Wenzel equation shows an enhanced contact angle. Thus, when $\theta_E < 90°$, it makes surfaces more hydrophilic and conversely when $\theta_E > 90°$, it makes the surface more hydrophobic via the modification factor.

$$\cos\,\theta_{\mathrm{W}} = \mathrm{r}\,\cos\,\theta_{\mathrm{E}} \tag{2.12}$$

2.4.2 The Cassie-Baxter equation

The aforementioned wetting models describes contact angle behavior on a simple, chemically homogeneous surfaces. However, in order to study contact angles on surfaces with multiple chemical configurations with different surface chemistries, Cassie proposed a law describing apparent contact angle for a heterogeneous surface as

$$\cos\,\theta_{\mathrm{C}} = \sum_{\mathrm{i}=1}^{\mathrm{N}} \phi_{\mathrm{i}}\cos\,\theta_{\mathrm{i}} \tag{2.13}$$

where, ϕ_{i} is the fractional surface area in contact with liquid and θ_{i} is the contact angle of the liquid on surface area for the i^{th} configuration

When the heterogeneous surfaces contain porous medium, $\theta = 180°$ for the second surface and the above equation becomes Cassie-Baxter equation given by Eq. 2.14. Liquid on top of surface does not penetrate and hence forms a spherical droplet as shown in Fig. 2.2d.

$$\cos\,\theta_{\mathrm{CB}} = \phi_1\cos\,\theta_1 - \phi_2 \tag{2.14}$$

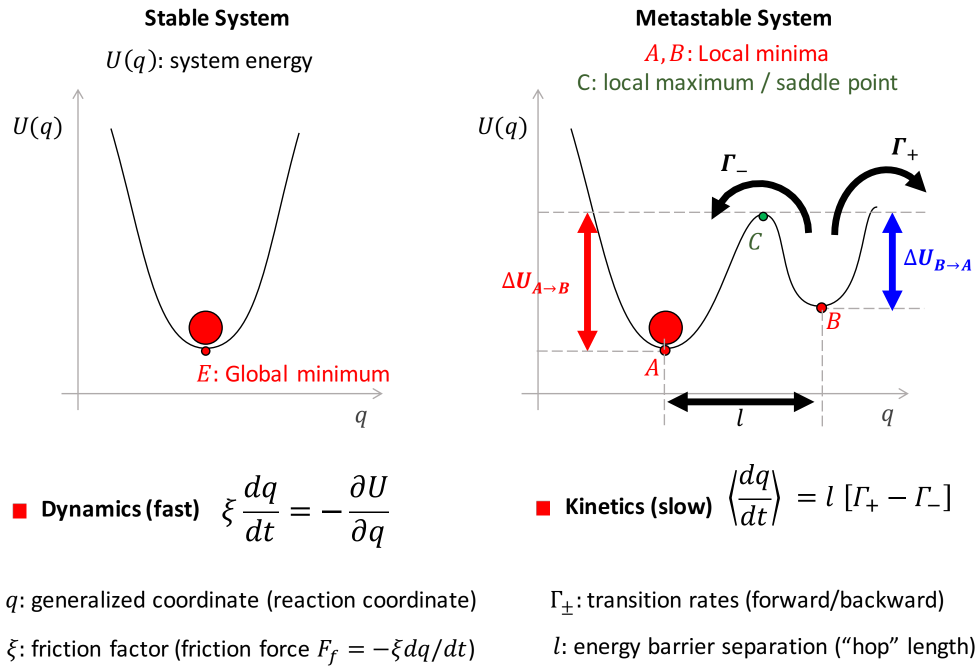

Figure 2.3: Dynamics and kinetics of thermodynamic system. (a) Stable system when there is a single minima where the relaxation to equilibrium is governed by the dynamic equation. (b) Metastable system when there are multiple energy minima. The relaxation to equilibrium is governed by transition hop rates governed by the kinetic equation.

2.5 Wetting transitions across different regimes

In a stable system, there is single energy minimum that is governed by the dynamic equation. For instance, dynamics of relaxation to the equilibrium for a perfectly smooth spherical particle close to the interface is governed by the balance of capillary forces with hydrodynamic friction. However, there exists multiple minima for the case of metastable systems thus there are transitions between the metastable systems which are governed by the kinetic equation such as in the case of sphere with heterogenities/defects. Both these systems are shown in Fig. 2.3.The transitions due to metastable states for a particle with nano-scale roughness results in crossover between relaxation regimes as noted by Colosqui et.al theoretically [58] and experimentally by Manoharan group [20].

Similar behavior was observed by Bibin et.al [22]for water droplet spreading in 100cSt PDMS silicone oil on borosilicate glass substrates. They reported very fast spreading

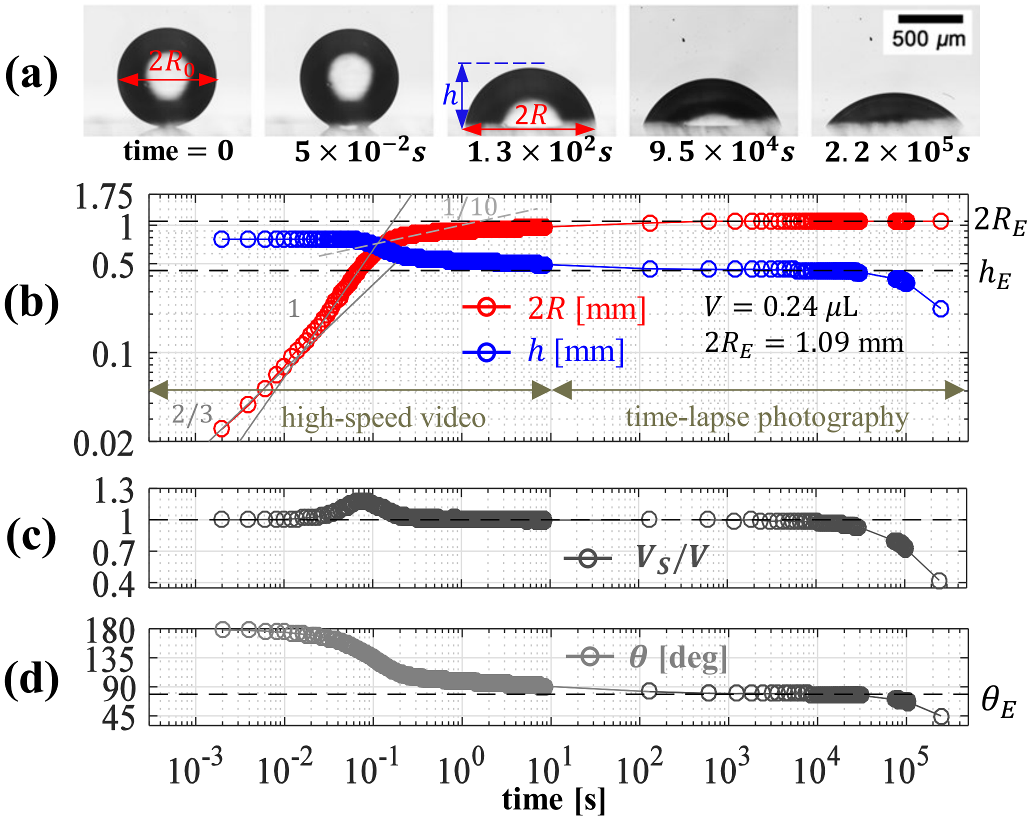

Figure 2.4: Wetting transitions on a borosilicate glass surface. (a) Time evolution of DI water droplet spreading in high viscous silicone oil (100-cSt). (b) Initial fast dynamics of contact radius (red) and height (blue) of the droplet is recorded using a high speed camera at 500 fps for the first 10 seconds followed by time-lapse photography at 500 sec interval to capture the entire evolution to mechanical equilibrium. (c,d) Volume V_S and contact angle θ corresponding to a spherical cap.

of water droplet upon deposition on the surface followed by a sudden change in wetting regime which was much slower and logarithmic in time as the equilibrium contact angle is approached (see Fig. 2.4). Thus surface roughness coupled with modifying the surfaces with lower surface energy materials, one can remarkably alter the wetting behaviors of the surfaces.

2.6 Physical ageing of spreading droplets in a viscous ambient phase

Classical continuum descriptions assumes interactions between liquid-liquid and liquid-solid pairs to be smooth, homogenous and neglects the presence of nanoscale hetero-

`AFM.pdf`

Figure 2.5: Nanoscale topography and model parameters. (a) Atomic Force Microscopy (AFM) 3D topographic image showing the details of borosilicate glass sample at nanoscale. (b) 1D local height (z) profile and the average height $\mathrm{z_a}$ of the glass surface. (c) Height autocorrelations for different locations $\phi = 0°, \pm 45°$. Vertical dashed line indicates the correlation length r_d corresponding to averaged topographic "defects" with base area $\mathrm{A_d} = 4.2\ \mathrm{nm}^2$. Inset illustrates a modeled conical "defect" with base area $A_d = \pi r_d^2$, height $\mathrm{z_a}$, and cross-sectional area ΔA_{wo}.

geneities, thermal fluctuations etc [51, 59, 60]. In this section, we report our work in spreading dynamics of water droplet in a high viscous silicone oil (100-cSt) ambience. While numerous groups previously studied water droplet in a low viscous medium, only a few studied the droplet dynamics in a high viscous oil. The droplet contact radius for the previous studies follows power law R(t) $\propto t^{\alpha}$ with variable exponents from $\alpha \simeq 0.1$ to 1 that present a nontrivial dependence on the viscosity of each phase. It has been shown, in particular, that the external phase viscosity can strongly influence the droplet spreading dynamics [61]. The different power laws observed in the dynamics of droplet spreading reflect the dominance of different physical mechanisms for energy dissipation and associated damping forces. Such damping forces have been commonly estimated using classical models for contact line dynamics such as the Voinov-Cox model, which considers viscous hydrodynamic friction, and the so-called molecular kinetic theory (MKT) [62], which considers that irreversible work is performed in the adsorption and desorption of molecules at a moving contact line. However, available models for contact line dynamics cannot account for the dynamic-to-kinetic regime crossover and extremely slow near-equilibrium relaxation reported for systems involving the displacement of liquid-liquid interfaces on a solid, as in the case of micro/nanoparticle adsorption and micro/nanocapillary imbibition.

Power-law behaviors with an expected range of exponents ($\alpha = 0.1$ to 1) are observed during the initial ~ 0.1 seconds of the spreading process, after which there is a crossover to an unexpectedly slow regime that persists for around 10^3 seconds until attaining the mechanical equilibrium condition. In order to understand the regime crossover, Colosqui et.al [22] proposed analytical model describing the presence of inherent nanoscale features/defects on the borosilicate glass gave rise to different metastable wetting states. We further studied the presence of the nanoscale defects via Atomic Force Microscopy (AFM) as shown in Fig. 2.5.

Atomic Force Microscopy (AFM) in non-contact mode was employed to produce (512 × 512 pixels) topographic images of 100 × 100 nm sections of the borosilicate glass substrates employed in the experiments (see Fig. 2.5a). The analysis of topographic profiles obtained via AFM reveals the presence of random nanoscale roughness having a nearly isotropic and Gaussian height distribution with average amplitude $z_a = 2\int_0^l |z| dx/l$

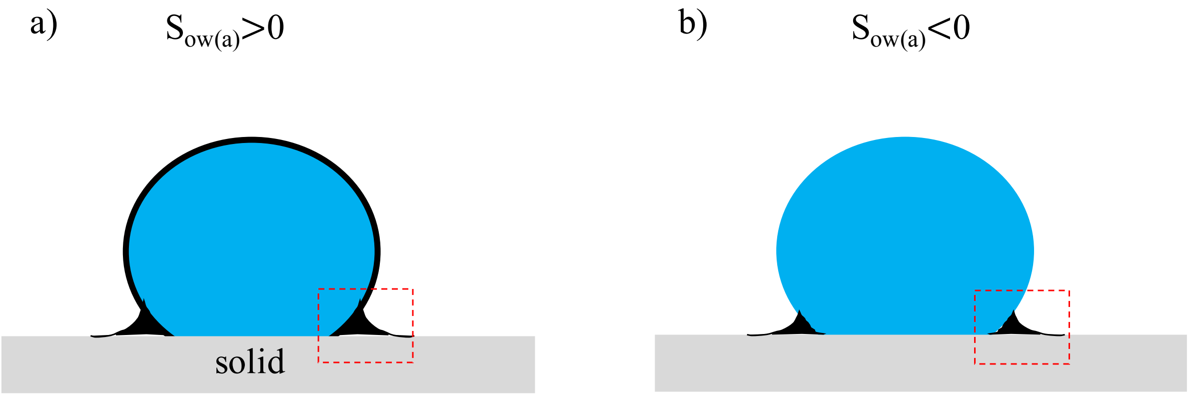

Figure 2.6: Behavior of lubricating oil for different spreading parameters a)oil(black) cloaks the water droplet(blue) b)oil forms a wetting ridge/meniscus with water droplet:reproduced this sketch from original paper [2]

= 0.6 nm (see Fig. 2.5b), standard deviation $\sigma \simeq$0.75 nm, small positive skewness $\zeta \simeq$ 0.3, and excess kurtosis $\kappa \simeq 0.1$.

The radial autocorrelation function C(r) = $\lim_{l\to\infty} \int_0^l z(\tau)z(\tau+r)d\tau/l$ computed from AFM data (Fig. 2.5c) shows a similar nearly exponential decay in different directions $\phi =$ atan(y/x). Notably, the decay of the height autocorrelation function is characterized by a correlation length $r_d \simeq 1.16$ nm, which indicates that topographic features approximately have the average base area $A_d = \pi r_d^2 \simeq$4.2 nm employed for analytical expression thus confirming the presence of defects as predicted by the analytical model . Topographic images of borosilicate glass slides employed in the spreading experiments were performed at the Center for Functional Nanomaterials in Brookhaven National Laboratory. Measurements were performed using a Park NX-20 AFM in Non-Contact (NC) mode and cantilever probes PPP-NCHR by Park Systems.

2.7 Liquid infused surfaces(LIS)

Liquid transport through micro channels underlies a plethora of technological applications, including drag reduction [57],energy storage and conversion [63], coatings [64]. Specifically fabrication of super-hydrophobic surfaces via plasma etching, organic materials, block copolymer self-assembly and nano-structures [26, 56] yields very high advancing contact angle (166°). We are interested in designing and performance of surfaces which separates water and oil (Hexadecane) at different hydrostatic pressures via laser patterning (see chapter 4). The inspiration being pattern surfaces with infused liquid showed remarkable robustness when it comes to repelling other immiscible liquids in contact. For instance, Stone et.al proposed a method using a flowcell with liquid infused surface patterns subjected to external shear.They performed theoretical prediction to quantify the wetted length rate and observed that aspect ratio of patterned grooves plays a significant role in the oil retention inside the patterned grooves [47]. Wong et.al developed an innovative technique fabricating Slippery liquid-infused porous surfaces (SLIPS) that repels liquids with varying surface tensions and possess very low contact angle hysteresis by using silanized epoxy substrates via replica molding method (REM). They demonstrated hydrophobicity of their surfaces in a highly pressurized Nitrogen environment which is equivalent to hydrostatic pressure at a depth of 7km thus exhibiting unprecedented robustness of the process [39]. Moreover, the surfaces repelled crude oils as well as blood and ice thus demonstrating omniphobicity which can have applications in anti-sticking. Another group Lynn et.al fabricated SLIP surfaces via multilayered Nano porous polymers for application in the field of biofouling paints .They successfully demonstrated the robust nature of the designed slippery surfaces that rolls liquids upon the deposition at tilt angles as low as 2° with very low contact angle hysteresis (2°). Furthermore, the sliding behaviors (thus the contact angles) of droplets on the surface can be manipulated via interactions between DI water with amphiphiles and thermotropic Liquid crystals used for infusion in the patterns. Most importantly, they demonstrated that trajectory of the deposited water droplet can be controlled via strategic positioning of pattern sticks and primary amines on the surfaces infused with oils [65]. These surfaces most commonly referred to as stick-slip surfaces contains the sticky patches to control the path without losing it's slippery nature. Seemann et.al proposed a novel technique to fabricate rectangular grooves with varying aspect ratios for studying the interplay between the large variety of liquid morphologies such as droplets, wedges and filaments inside the grooves and contact angle with substrate. The proposed technique was also used to manipulate contact angles under external applied electric field thus focusing on application in the area of electrowetting [66].

Smith et.al described hydrodynamic principles for liquid penetration in the surfaces and determined 12 thermodynamic conditions to describe the four phase system consisting of solid substrate, lubricating liquid(usually oil), probing liquid (water) and air. When the spreading parameter $S_{ow(a)} > 0$, the lubricating oil completely covers the deposited water droplet (see Fig. 2.6a) in order to reduce the surface energy however oil forms a meniscus with droplet if $S_{ow(a)} < 0$ as shown in Fig. 2.6b. It is given by

$$S_{ow(a)} \equiv \gamma_{wa} - (\gamma_{ow} + \gamma_{oa}) \tag{2.15}$$

where γ_{wa} is the water -air surface tension, γ_{ow} is the oil-water surface tension and γ_{oa} is the oil-air surface tension.

Depending on spreading parameter, there are different wetting states and hence the system presents varying thermodynamic conditions. For example, water droplet can completely wet the surface, partially wets the surface or has no contact with the surface near the droplet-oil interface [44]. In any case, the previous work on LIS [2,44] suggested three criteria must be met for designing a robust liquid infused surface, moreover they made following observations by studying all the possible thermodynamic wetting states. They are i) the droplet can fall into a Wenzel state and pin on the substrate if the lubricant is not present underneath the probing droplet ii) probing droplet prefers to slide but interactions with the solid will cause frictional forces if the oil is only partially covered iii)if the lubricant does not encapsulate or impregnate the surface, eventually the droplet will reach a dry surface and get pinned. We are interested in learning wetting behaviors of water infused laser patterned surfaces. In chapter-4, we explore both statics and dynamics of different liquids inside the laser patterned slit channels with a potential for application in water-oil separation.

2.8 Theoretical model for wetting in LIS

Our studied capillary device (Fig. 4.1a) consists of a 3D slit channel of length ℓ with a rectangular cross section of width w and narrow height $h \ll w$, that is filled with two immiscible fluids A and B having an interfacial tension $\gamma = \gamma_{AB}$. The slit channel has two sections 1 and 2 having different effective surface energies γ_{A1}, γ_{A2} and γ_{B1}, γ_{B2} when wetted by fluid A and B, respectively. Hence, the surface energy difference

$\Delta\gamma_i = \gamma_{Ai} - \gamma_{Bi}$ determines the Young contact angle $\cos\theta_i = -\Delta\gamma_i/\gamma$ for each section $i = 1, 2$. The junction between the two different sections of the slit having lenghts L_1 and L_2, respectively, is located at a distance $z_j = L_1 - d$ measured from the flat interface at $z = 0$, when the leading edge of the slit is immersed at a depth d (Fig. 4.1a).

This analysis will focus on the case of vertical imbition (Fig. 4.1a) where the capillary diode is in contact with a large bath of fluid A and capillary action, when $\theta_1 \leq \theta_2 < 90°$, drives phase A upward against the action of gravity. As the fluid phase A displaces phase B, the average position of the three-phase contact line $z = (1/\mathcal{S}) \times \int_0^{\mathcal{S}} f(s)ds$ is given by averaging the local contact line position $f(s)$ (Fig. 4.1a) along the full contact line perimeter $s = 0, \mathcal{S} = 2(w + h)$. We will consider that the closed system comprising the capillary slit and the fluid phases A and B is in thermal and chemical equilibrium. Furthermore the fluids A and B are considered to be incompressible with a constant mass density ρ_A and ρ_B, respectively. The system free energy parameterized by the average contact line position can be thus expressed as

$$\mathcal{U}(z) = \frac{1}{2}\Delta\rho g w h z^2 + \gamma w h \frac{(\pi - 2\theta)}{2\cos\theta} + 2\Delta\gamma(z)(w + h)z \tag{2.16}$$

where $\Delta\rho = \rho_A - \rho_B$ is the mass density contrast, g is the gravitational acceleration, θ is the apparent contact angle at the three-phase contact line, and

$$\Delta\gamma(z) = -\gamma\cos\theta_1 + \frac{\gamma}{2}(\cos\theta_1 - \cos\theta_2)\left[1 + \tanh\left(\frac{z - z_j}{\delta}\right)\right] \tag{2.17}$$

is the surface energy difference, which is modeled as having a gradual spatial variation centered at z_j and over a finite distance $\delta = (1/\mathcal{S}) \int_0^{\mathcal{S}} (f(s) - z)^2 ds$. The amplitude of spatial variations $|f(s) - z|$ of the local contact line position is determined by a balance between surface and gravitational energy and thus $\delta = \ell_c g(\theta)$, where $\ell_c = \sqrt{\gamma/\Delta\rho g}$ is the capillary length and $g(\theta) \sim \mathcal{O}(1)$ is a shape factor that is close to unity for $w \gg \ell_c$ and $\theta \ll 1$.

Under the modeled conditions, the effective driving force for the displacement of the average contact line position is $F(z) = -\partial\mathcal{U}/\partial z$. The global minimum of the free energy $\mathcal{U}$ in Eq. 4.1, and thus the stable equilibrium condition, is located at $z_E = (2\gamma\cos\theta_2/\Delta\rho g) \times (1/h + 1/w)$ provided that z_j is sufficiently smaller than z_E. Moreover, Eqs. 4.1–4.2 predict

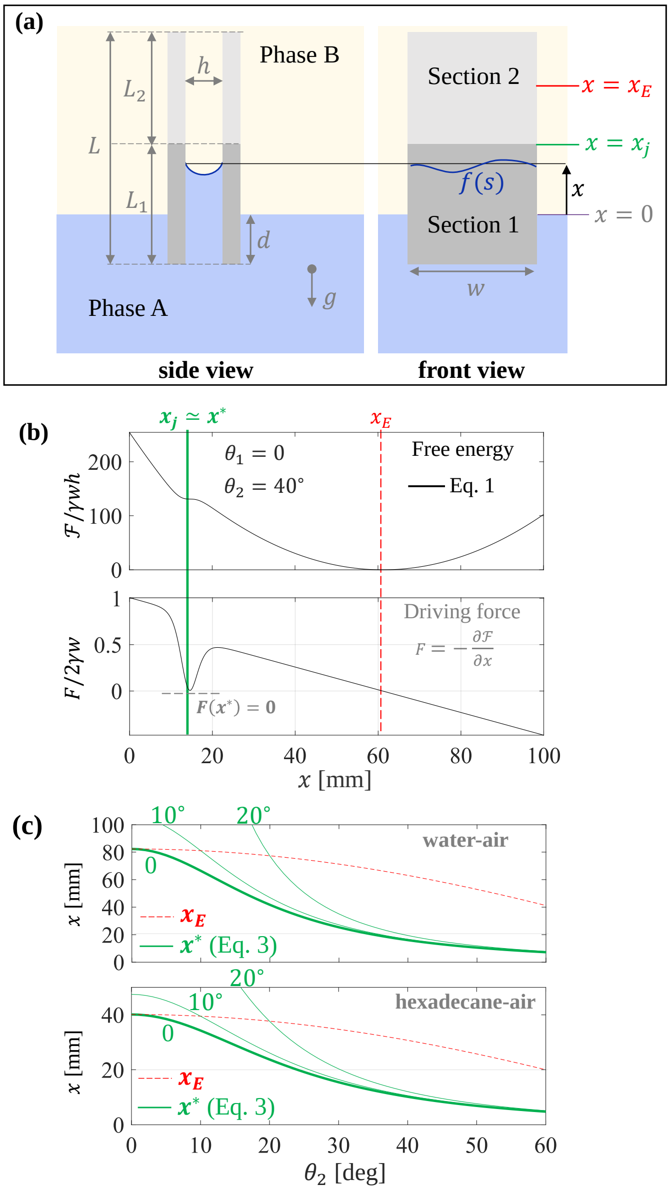

Figure 2.7: Device design and analytical description. (a) Vertical imbibition of a capillary slit with two sections having Young contact angles θ_1 and θ_2 prescribed by their effective surface energies. (b) Dimension system free energy and driving force predicted by eq 4.1 for water-air ($\theta_1 = 0°$ and $\theta_2 = 40°$) and a slit channel with the section junction at $z_j = z^\star = 14$ mm and $\delta = l_c$. (c) Critical junction position for producing metastability predicted by eq 4.3 for $\theta_1 = 0°, 10°, 20°$ and $\theta_2 = 0° - 60°$ in the case of water ($\rho = 997$ kg/m^3, $\gamma = 72$ mN/m) or hexadecane oil ($\rho = 770$ kg/m^3, $\gamma = 27$ mN/m) in ambient air.

a local energy minimum at the critical value

$$z^* \simeq (\cos\theta_1 + \cos\theta_2) \times \left[\frac{\Delta\rho g}{\gamma(1/h + 1/w)} + \frac{(\cos\theta_1 - \cos\theta_2)}{\delta}\right]^{-1}. \tag{2.18}$$

As shown in Fig. 4.1b for the particular case of $\theta_1 = 0$ and $\theta_2 = 40°$, when the position of the junction $z_j \geq z^*$ is equal or larger than the critical value defined by Eq. 4.3 the capillary imbibition of liquid will stop at a metastable equilibrium position for which $F(z^*) = 0$ and there will be no conduction of fluid inside the slit beyond that point. The metastable equilibrium at $z = z^* < z_E$ with no fluid conduction will be observed for long observation times, provided that the energy barrier to cross the junction $\Delta\mathcal{U} \simeq 2\gamma|\cos\theta_2 - \cos\theta_1|(w+h)z_j \gg k_BT$ is orders of magnitude larger than the thermal energy k_BT and the assumption of chemical and thermal equilibrium leading to Eq. 4.1 is valid (e.g., when evaporation and surface condensation is not significant).

Analytical predictions from Eq. 4.3 for the critical junction position to produce metastable equilibrium are reported in Fig. 4.1c for the case of water or hexadecane oil in a microscale slit of height $h = 180$ μm and width $w \gg h$ with a liquid-infused and conventional surface for which $\theta_1 \simeq 0$, 10, or 20° and $\theta_2 =$ 20-60°, respectively, and assuming $\delta = \ell_c$ is determined by the capillary length for each liquid pair. Placing the junction position at 20 mm above the flat interface (Fig. 4.1c) will stop the capillary imbibibtion of water when $\theta_1 \lesssim 20°$ and $\theta_2 \geq 35°$, which are equilibrium contact angles within the range commonly observed for water on hydrophilic surfaces such as micropatterned or conventional glass. For same slit geometry and type of surfaces, the equilibrium contact angles of hexadecane or other oils are expected to be significantly lower ($\theta_1 \simeq \theta_2 \leq 20°$) and the capillary conduction of oil will be able continue above the junction until reaching the stable equilibrium state at $z_E > z^*$ or fill the entire slit when $L \leq z_E$.

Analytical predictions from Eq. 4.3 for the particular conditions reported in Fig. 4.1c thus indicate that a simple prototype device with $z_j \simeq 20$ mm can prevent the vertical capillary imbibibition of water into the second section where $z > z_j$, while oil can readily flow over the junction and fill the second section of the slit. Both water or oil can flow over the junction if its position is reduced to $z_j = 10$ mm, which can be readily accomplished by immersing the edge of the device at $d = 10$ mm inside the fluid bath (Fig. 4.1a). This analytical finding suggests a possible strategy for separation of water from a mixture of water and a less dense oil by immersing in the mixture the analyzed capillary device at controlled depths for which only one or both phases can flow continuously through the slit channel.

In particular, a device with a first superhydrophilic section filled with water can be potentially employed as a fluidic diode preventing spontaneous or forced imbibition by any liquid below a threshold pressure head $\Delta p^* = \Delta\rho g(z_E - z^*) > 0$ across the slit channel. These analytical predictions will be tested through the fabrication procedure and experimental analysis reported in the chapter-4.

2.9 The Navier-Stokes equation

The Navier-Stokes equation describes the motion of liquids in confinements such as pipes, tubes and rectangular channels etc. It is used to describe mathematically the conservation of mass (the continuity equation) and the conservation of momentum.

The momentum equation is given by

$$\rho\frac{\mathrm{D}\mathbf{u}}{\mathrm{Dt}} = -\nabla \mathrm{p} + \nabla\cdot\tau + \rho\mathbf{g} \tag{2.19}$$

where ρ is the density of the liquid, τ is the stress tensor, $\mathbf{u}$ is the flow velocity, p is the pressure, $\nabla\cdot$ is the divergence, $\mathbf{g}$ is the gravity and $\frac{D}{Dt}$ is the material derivative. The generalized momentum equation Eq. 2.19 can be expressed in cartesian (x,y,z), cylindrical (r, θ, z) and spherical (r, θ ,ϕ) coordinates. These equations can be used to obtain flow velocity profiles and flow rates of liquids in cylindrical and rectangular channels under certain assumptions for the flow which is discussed in the next subsections.

2.9.1 Poiseuille flow in cylindrical channels

Flow profiles for a newtonian fluid inside a cylindrical capillary can be obtained using the r-component,

$$\rho\left(\frac{\partial u_r}{\partial t} + u_r\frac{\partial u_r}{\partial r} + \frac{u_\theta}{r}\frac{\partial u_r}{\partial\theta} - \frac{u_\theta^2}{r} + u_z\frac{\partial u_r}{\partial z}\right) = -\frac{\partial p}{\partial r} + \left[\frac{1}{r}\frac{\partial}{\partial r}\left(r\tau_{rr}\right) + \frac{1}{r}\frac{\partial\tau_{r\theta}}{\partial\theta} - \frac{\tau_{\theta\theta}}{r} + \frac{\partial\tau_{rz}}{\partial z}\right] + \rho g_r \tag{2.20}$$

the θ-component,

$$\rho\left(\frac{\partial u_\theta}{\partial t} + u_r\frac{\partial u_\theta}{\partial r} + \frac{u_\theta}{r}\frac{\partial u_\theta}{\partial\theta} + \frac{u_r u_\theta}{r} + u_z\frac{\partial u_\theta}{\partial z}\right) = -\frac{1}{r}\frac{\partial p}{\partial\theta} + \left[\frac{1}{r^2}\frac{\partial}{\partial r}\left(r^2\tau_{r\theta}\right) + \frac{1}{r}\frac{\partial\tau_{\theta\theta}}{\partial\theta} + \frac{\partial\tau_{\theta z}}{\partial z}\right] + \rho g_\theta \tag{2.21}$$

and the z-component

$$\rho\left(\frac{\partial u_z}{\partial t}+u_r\frac{\partial u_z}{\partial r}+\frac{u_\theta}{r}\frac{\partial u_z}{\partial \theta}+u_z\frac{\partial u_z}{\partial z}\right)=-\frac{\partial p}{\partial z}+\left[\frac{1}{r}\frac{\partial}{\partial r}\left(r\tau_{rz}\right)+\frac{1}{r}\frac{\partial \tau_{\theta z}}{\partial \theta}+\frac{\partial \tau_{zz}}{\partial z}\right]+\rho g_z \tag{2.22}$$

Let us consider an incompressible ($\nabla \cdot \mathbf{u}=0$) and steady state ($\frac{\partial()}{\partial t}=0$) liquid flowing in a cylinder. Furthermore, the following assumptions $\frac{\partial p}{\partial z}=const$, $\frac{\partial u_z}{\partial \theta}=0$ and $u_r=u_\theta=0$ reduces the Eqs. 2.20–2.22 to

$$-\frac{\partial p}{\partial r}+\rho g_r=0 \tag{2.23}$$

$$-\frac{1}{r}\frac{\partial p}{\partial \theta}+\rho g_\theta=0 \tag{2.24}$$

$$-\frac{\partial p}{\partial z}+\eta\frac{1}{r}\frac{d}{dr}\left(r\frac{du_z}{dr}\right)+\rho g_z=0 \tag{2.25}$$

Using the Eqs. above, one can obtain the general solution for a flow in a capillary channel as

$$u_z=\frac{1}{4\eta}\left(\frac{\partial p}{\partial z}-\rho g_z\right)r^2+c_1 lnr+c_2 \tag{2.26}$$

where η is the dynamic viscosity of the liquid.

Applying the boundary conditions a) $u=0$ at $r=R$ b) $c_1=0$ at $r=0$ since the velocity is finite leads to

$$u_z(r)=v_0\left[(1-\left(\frac{r}{R}\right)^2\right] \tag{2.27}$$

the Hagen-Poiseuille equation.

The volumetric flow rate is obtained by integrating the velocity profile with respect to radius r from r = 0 to r = R

$$Q=\frac{\pi R^4}{8\eta}\frac{dp}{dx} \tag{2.28}$$

where R is the radius of the capillary and x is the length of the capillary channel.

2.9.2 Flow in rectangular channels

Assuming an incompressible ($\nabla \cdot \mathbf{u} = 0$), steady state ($\frac{\partial ()}{\partial t} = 0$) and fully developed liquid flowing in a rectangular box of width W and height H, the x-momentum Navier-Stokes equation is given by

$$\mu \left(\frac{\partial^2 u_x}{\partial y^2} + \frac{\partial^2 u_x}{\partial z^2} \right) = \frac{\partial p}{\partial x} \tag{2.29}$$

Using no-slip boundary conditions at the wall, velocity profile is obtained

$$u_x(y, z) = -\frac{1}{2\eta} \frac{\partial p}{\partial x} f_s(y, z) \tag{2.30}$$

with, $f_s = \left(\frac{H^2}{4} - y^2 \right) - \sum_{n=0}^{\infty} a_n cos \left(\frac{\lambda_n y}{H/2} \right) cosh \left(\frac{\lambda_n z}{H/2} \right)$ where a_n is the number of modes and $\lambda_n = \frac{(2n+1)\pi}{2}$.

Volumetric flux can be obtained by integrating flow profile which gives

$$Q = -\frac{WH^3}{12\mu} \frac{\partial p}{\partial x} f_Q \left(W/H \right) \tag{2.31}$$

where, $f_Q = 1 - 6\frac{W}{H} \sum_{n=0}^{\infty} \lambda_n^{-5} tanh \left(\lambda_n W/H \right)$.

Chapter 3

Liquid transport characterization via X-ray Photon Correlation Spectroscopy

This Chapter describes the experimental work and numerical analysis performed to developed a method to employ XPCS for characterizing fluid transport properties such as the velocity flow profile, volumetric flow rate, and rheological properties of liquids that are forced to flow through a capillary tube or microfluidic channel. X-rays are a good probe to understand the phenomenon of condensed matter systems at nanoscale. In this dissertation, I will discuss the dynamics of colloidal systems as a whole. This could be achieved by measuring the superposition of the diffracted waves from each scatterer which produces an interference pattern. The resultant interference pattern after the sample is probed by an incoming beam contains the information about both the static and dynamic properties of the sample. Hence, the fluctuation in the interference pattern corresponds to the dynamics of system of interest. This is precisely what the relatively young technique X-ray Photon Correlation Spectroscopy (XPCS) measures.

Dynamic Light Scattering (DLS), which is analogous to XPCS can also be used to measure the coherent diffraction from the samples, though it is constrained to the visible spectrum. However, the XPCS technique can measure the changes at very small wavelengths ($\sim 1\AA$), which opens up wide variety of system configuration such as colloidal dynamics near glass transition, dynamics in dense suspensions [67, 68] and dynamics of polymer systems [11,69,70] etc to characterize. This research is focused on characterizing flow profiles of colloidal suspensions in microcapillaries. Many techniques were proposed in the past such as Particle Image Velocimetry (PIV) and Laser Doppler Velocimetry which studies flow profile distribution in closed confinements by following the trajectory of tracer particles [7]. However, these techniques can not be used to study opaque samples and they can only probe systems at larger wavelengths, hence lower resolution. This is where the smaller wavelength x-ray probe technique such as X-ray Photon Correlation Spectroscopy plays a major role.

The XPCS experiments have been conducted at the Brookhaven National Laboratory National Light Synchrotron Light Source II (NSLS-II) in collaboration with Dr. Andrei Fluerasu at the coherent hard x-ray (CHX) beamline. The method known as XPCS is a spectroscopy technique based on x-ray scattering, that enables probing length scales typically ranging from nanometers to microns and time scales ranging from microseconds to minutes.

This PhD research project involved a fair bit of programming. All the data analysis pipelines were programmed in Jupyter Notebook in Python. The code is included at the end of this document for reference.

3.1 Experimental method

X-ray scattering involves illuminating the sample of interest with an x-ray beam. During the scattering, electrons in the shells are excited by the incoming photons which results in emanating spherical waves. The result is angular distribution of the scattered x-rays. A typical x-ray scattering is shown in Fig. 3.1. The x-rays with incoming wave vector $\overrightarrow{k_i}$ scatter with wave vector $\overrightarrow{k_f}$ which is measured by a detector at a position $\overrightarrow{q} = \overrightarrow{k_i}$ - $\overrightarrow{k_f}$.

In an elastic scattering, the energy of each photon interacting with the matter does not change unlike in the Raman scattering. In this scenario, let I be the intensity of incident x-rays (photons/s) and A is the detector area. The intensity per area measured has the units of power per unit area. This quantity is related to electric field via the time average of the Poynting vector, which for EM waves in vacuum, is:

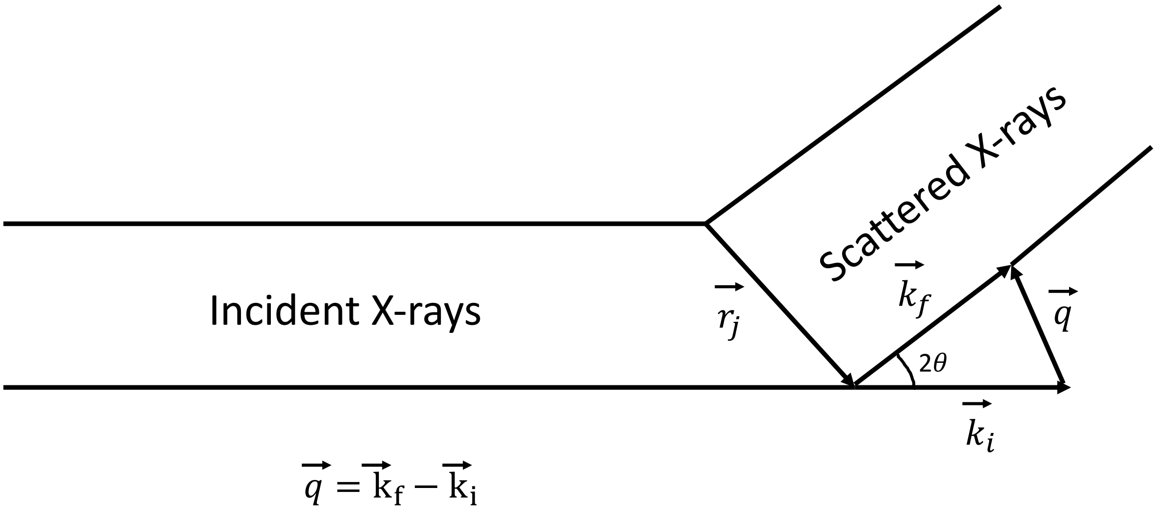

Figure 3.1: Sketch of the x-ray scattering process showing the incident x-rays $\mathbf{k}_i$ scattered by the sample at an angle 2θ with the wave vector $\mathbf{k}_f$ and the resultant vector $\mathbf{q}$ measured at a detector.

$$\langle S \rangle = \frac{c}{2} \left| \mathbf{E}(\mathbf{q}, t) \right|^2 . \tag{3.1}$$

The XPCS experiments in this work were performed in a small angle X-ray scattering (SAXS) geometry. A double crystal monochromator Si (111) was used to select 9.6 keV x-rays with a relative bandwidth $\frac{\Delta\lambda}{\lambda} = 10^{-4}$. The liquid sample in the flow cell was placed at a distance of 10.18 m from the detector. The parasitic scattering from beam is prevented by the position of guard slits, final coherent flux in the sample was 10^{11} ph/s. The scattering was recorded with a 2 dimensional (2D) sensor-Eiger 4M detector. As the name indicates, sensor can record images of size 2000×2000 pixels. The experiments were carried at 750 frames/sec at an exposure time of 1.34 milli-sec. Under these conditions, the speckle contrast was $\sim 20\%$.

The intensity autocorrelation functions,

$$g^{(2)}(\mathbf{q}, t) = \frac{\langle I(\mathbf{q}, t_0) I(\mathbf{q}, t_0 + t) \rangle}{\langle I(\mathbf{q}, t_0) \rangle^2} \tag{3.2}$$

were calculated via multi-tau correlator package in Python to study the decay of autocorrelations due to various relaxation processes of condensed matter systems at the CHX beamline.

The time averaged second-order intensity autocorrelations $g^{(2)}(\mathbf{q},t)$ is related to the normalized intermediate Scattering Function (ISF) via the Siegert relationship [3]:

$$g^{(2)}(\mathbf{q},t) = 1 + \beta . \left|g^{(1)}(\mathbf{q},t)\right|^2 . \tag{3.3}$$

Homodyne correlation functions for XPCS experiments under continuous flow in Poiseuille configuration has the following analytic form

$$\left|\mathrm{g}^{(1)}(\mathbf{q},\mathrm{t})\right|^2 = \exp(-2\mathrm{Dq}^2\mathrm{t}) \; \frac{\pi}{8\mathrm{qvtcos}\phi} \left|\mathrm{erf}\left(\frac{1+\mathrm{i}}{2}\sqrt{\frac{4\mathrm{qvtcos}\phi}{\pi}}\right)\right|^2 \; \exp(-\mathrm{v}_{\mathrm{tr}}\mathrm{t})^2, \tag{3.4}$$

where $\mathbf{q}$ $[\mathring{A}^{-1}]$ is the scattering wave vector or momentum transfer, $\mathbf{v}$ is the flow velocity, D is the tracer diffusion coefficient, $\phi = 90^\circ - \phi_0$ is the angle between $\mathbf{q}$ and flow direction $\mathbf{v}$ ((ϕ_0 is the orientation of the $\mathbf{q}$ ring in the counter clockwise direction measured from the positive x-axis).

The Eq. 3.4 can be expressed as

$$\left|\mathrm{g}^{(1)}(\mathbf{q},\mathrm{t})\right|^2 = \left|\mathrm{g}_{1,\mathrm{D}}\,(\mathbf{q},\mathrm{t})\right|^2 \; \left|\mathrm{g}_{1,\mathrm{S}}\,(\mathbf{q},\mathrm{t})\right|^2 \; \left|\mathrm{g}_{1,\mathrm{T}}\,(\mathbf{q},\mathrm{t})\right|^2. \tag{3.5}$$

The expressions Eqs. 3.4&3.5 show that the intensity autocorrelation functions depends on three components. The first term (subscript D) describes an exponential decay in time due to microscopic dissipative dynamics. The second term (subscript S) describes the decay due to variations of the local velocity field associated with viscous shear. The final term (subscript T) gives the relaxation rate due to the transit velocity of the particles. The relaxation times corresponding to the free diffusion coefficient and shear are very small ($\sim 10^{-2}$sec), compared to the decay due to transit times (∼0.6 sec). Therefore, the last term can be neglected [3] for fitting the x-ray data.

3.2 Liquid sample and flow cell preparation

Silicon dioxide (SiO_2) colloidal spheres of nominal diameter 250 nm (purchased from Duke Scientific) were dispersed in water and Polysorbate 20, a non-ionic surfactant commercially known as Tween 20 (purchased from Sigma-Aldrich), was used for stabilizing solutions.

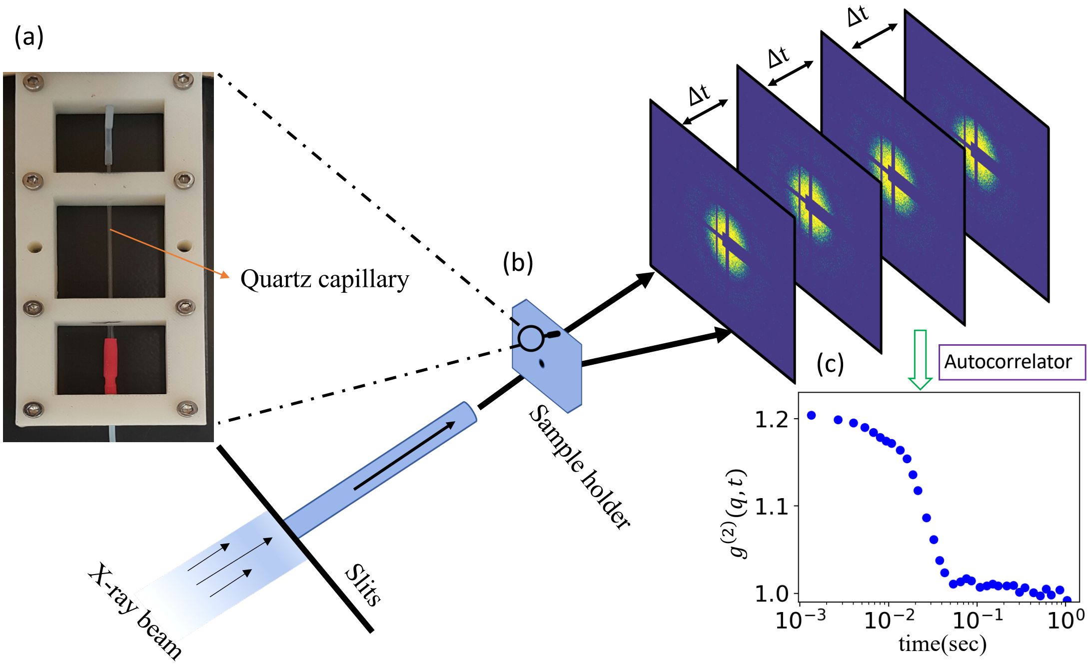

Figure 3.2: XPCS experimental setup.(a) Custom-built sample holder for flow experiments.(b) Sketch of XPCS experiment with scattering images at different time.(c) Intensity fluctuation autocorrelation functions obtained from the image time series.

Tween 20 was mixed with the spherical nanoparticles in the ratio of 2:1 and placed in a stirrer to ensure proper mixing. The sample was placed in a sonicator for one hour to remove bubbles formed during the mixing. The dynamic viscosity of the sample $\mu = 0.44$ Pa-sec was measured using a rheometer.

The custom-built flow cell shown in Fig. 3.2a was assembled using flow tubes, leak-tight fittings and adapters, and a quartz capillary with an outer radius of 0.5 mm and wall thickness ≈ 100 μm. A syringe pump is used to push the sample solution at flow rates ranging from $Q = 0$ to 2 μL/min, which corresponds to average flow velocities $v_0 \approx 0 - 66\mu$m/sec. The corresponding Reynolds number is $\text{Re} = \rho\, v_0 D/\mu < 10^{-4}$, where ρ is the liquid mass density and μ is the dynamic viscosity. Under these conditions, the fluid is Newtonian and the flow is laminar. The flow cell chamber was mounted at an angle normal to the x-ray beam direction, therefore the sample inside the capillary flows at 90° with respect to the horizontal plane. The flowing sample is illuminated by the x-ray beam in all directions thus the scattered data contains information of the sample structure in all orientations.

The scattering data of the flowing sample for each measurement was stored as a Unique Identification number (UID) in the photon detector. The images from the detector were accessed from the python pipelines setup for data analysis in a Jupyter notebook. Based on the signal frequency of the XPCS experiments, regions of interest (ROI) were obtained with the width of each region or "slice" ∼13° as shown in Fig. 3.3a. An Eiger 4M detector can characterize the dynamics of complex colloidal liquids in the order of 1 millisec. Hence, non-equilibrium processes for higher momentum transfer ($\mathbf{q} > 5 \times 10^{-3} \mathring{A}^{-1}$) were hard to capture owing to their faster correlation times, which would require a higher frequency detector such as 500KHz.

3.3 Experimental intensity autocorrelation and analytical fitting

In previous work [3, 8], the correlation times were calculated only for two orientations by taking advantage of the anisotropy of the autocorrelation functions. One, when the scattering wave vector ($\mathbf{q}$) is aligned in the direction of bulk motion ($\mathbf{v}$) and the other, when it is normal to the flow direction. Thus, parameters such as the flow velocity and diffusion coefficient obtained by fitting the x-ray data correspond to non-equilibrium processes only for two local configurations; i.e., $\mathbf{q} \parallel \mathbf{v}_0$ and $\mathbf{q} \perp \mathbf{v}_0$. It does not describe macroscopic dynamics of colloidal suspensions for the entire ROI in the detector. Therefore, we take a new approach of synthesizing the experimental auto-correlation functions of the ROI, which will be referred as $g^{(2)}_{expt}$ and subsequently fit the entire data at once using the analytic equation Eq. 3.4. The procedure is described below.

Data fitting was performed in two steps. In the first step, fitting parameters such as the local flow velocity, free diffusion coefficient, beta (β) and baseline(g_∞), were obtained for each individual region or "slice" by fitting the x-ray data $g^{(2)}_{expt}$ with the analytic equation Eq. 3.4. In our analysis, we selected three scattering wave vector ($\mathbf{q}$) rings and ten orientations (ϕ_0). Therefore, we totally have 30 different configurations (see Fig. 3.3a)and the fitting parameters for each configuration were obtained in data analysis.

Since the free diffusion coefficient, which is a measure of dissipative dynamics of the colloidal suspension is prescribed by the viscosity of the sample and, flow velocity parameter is characteristic of bulk flow, we fit the data of entire ROI in the next step at once in order to obtain flow behavior of the colloidal suspension under continuous flow. Therefore, $g^{(2)}_{expt}$ for all the regions ($\phi's$) and scattering wave vectors ($\mathbf{q}$) are selected for fitting the x-ray data second time with equation Eq. 3.4. Regression analysis was performed in the non-linear least squares sense by using parameters beta and baseline from the first step to compute the residues and obtain the best fit for data. Examples of experimental data with fits are shown in Fig. 3.3b-d. In this process, average flow velocity v_0 and free diffusion coefficient D_0 are obtained.

In conclusion, the x-ray data agrees well with the analytic equation which assumes a parabolic flow shape for the XPCS studies in a cylindrical capillary. However, determine the flow profile when no a priori information on the liquid employed is available requires fitting the intensity autocorrelations through numerical optimization. In the next section, we discuss a method of obtaining flow profiles from numerical calculations via Fourier mode decomposition.

3.4 Experimental intensity autocorrelation and numerical fitting

3.4.1 Parametrization using Fourier modes

The experimental autocorrelation functions $g^{(2)}_{expt}$ can be used to obtain key parameters such as average flow velocity v_0 and free diffusion coefficient D_0 via fitting as described in previous section. In this work, we solve an inverse problem for obtaining velocity profiles from the x-ray data by using a Fourier mode decomposition. By representing the flow velocity profile by a finite set of Fourier modes we can significantly reduce the free parameters that must be optimize to obtain the best possible fit to the x-ray data.

The Fourier modes are determined according to

$$A_n = \frac{1}{R}\int_0^R v(r)cos\left(\frac{(n+1/2)\pi r}{R}\right)dr, \tag{3.6}$$

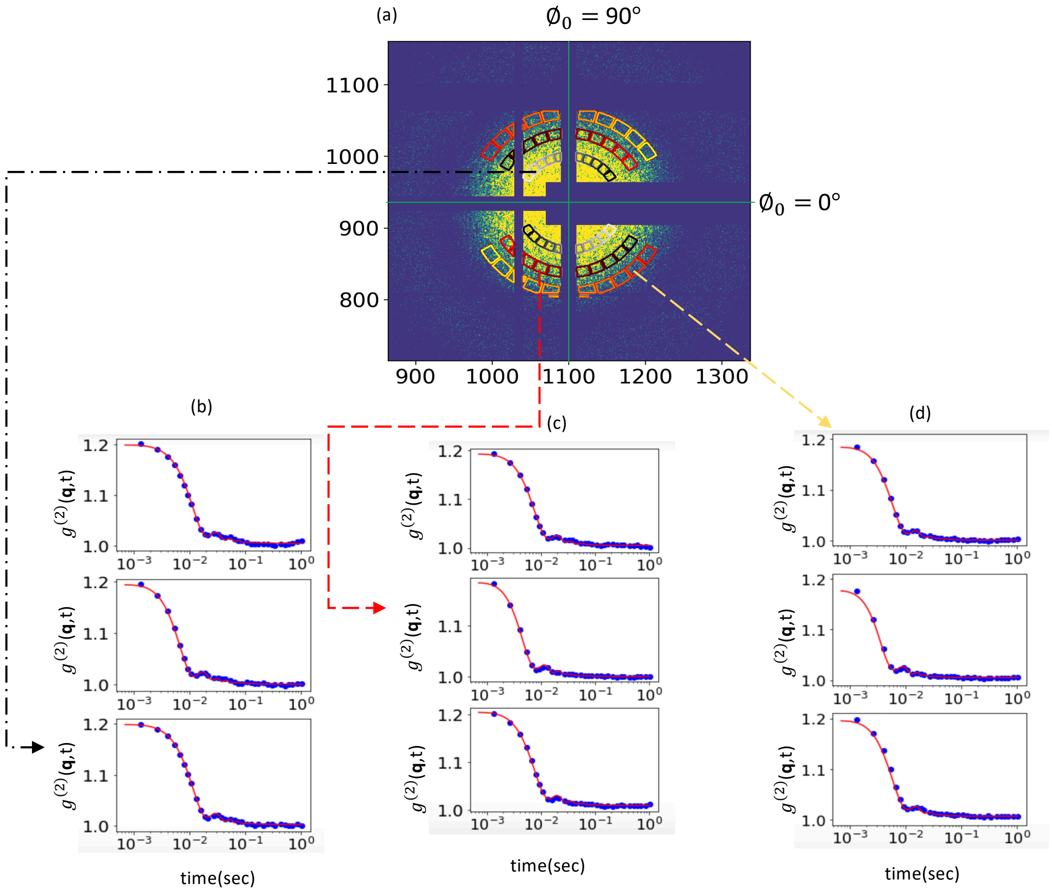

Figure 3.3: (a) Region of Interest (ROI) mask of different q rings and regions (ϕ_0) for data analysis. (b) Intensity autocorrelation functions $g^{(2)}$ of experimental data (blue circles) and analytic fit (red) using the Eq. 3.4 for the q ring $\mathbf{2.35}\times10^{-3}$ $\mathring{A}^{-1}$ and regions ϕ_0 35°(row 1), 101°(row 2)and 145°(row 3) respectively. (c) Experimental autocorrelations (blue circles) and analytic function (red) using the Eq. 3.4 for the q ring $\mathbf{3.5}\times10^{-3}$ $\mathring{A}^{-1}$ and ϕ_0 35°, 101° and 145° respectively. (d) Experimental autocorrelations (blue circles) and analytic function (red) using the Eq. 3.4 for the q ring $\mathbf{4.5}\times10^{-3}$ $\mathring{A}^{-1}$ and ϕ_0 35°, 101° and 145° respectively.

for n=0,1,2....N, which represents number of Fourier modes and,

$$v(r) = \sum_{n=0}^{\infty} A_n cos\left(\frac{(n+1/2)\pi r}{R}\right) \tag{3.7}$$

where R= radius of capillary, $v(r)$ is the flow velocity distribution inside the channel.

The velocity profile that corresponds to Poiseuille flow [71] is

$$v(r) = 2v_0\left(1 - \left(\frac{r}{R}\right)^2\right). \tag{3.8}$$

This flow profile can be accurately represented by a truncated Fourier series using the Eq. 3.6 to obtain an initial set of Fourier modes, which will be referred to as the parabolic flow modes, and is shown as green circles in the mode-space map in Fig. 3.4a. An array of Fourier modes is generated close to the initial parabolic flow modes so that the phase space for analysis captures various deviations from the parabolic flow profile. Each grid point (yellow circle) in the phase space is characterized by a distinct flow profile governed by the Eq. 3.7. In the neighborhood of the parabolic flow modes (blue, sky blue and violet boxes), flow profiles (red circles) obtained via Eq. 3.7 have nearly parabolic shapes at varying flow rates as shown in Fig. 3.4b-d. However, the flow profile has a plug flow shape for the grid point far from the parabolic modes set (green point in Fig. 3.4e). The inset plots for each case in Fig. 3.4b-e shows the experimental autocorrelations (blue circles) and, the numerical autocorrelations (red) which will be described in the following subsections.

3.5 Numerical determination of the intensity autocorrelation functions

After a region of mode space is defined, the number of Fourier modes required in the analysis needs to be determined. First, only one mode (A_0) is used to extract the flow profiles or velocity distribution. The numerical intensity autocorrelations are obtained using flow profiles (δv) determined by Eq. 3.9. The experimental autocorrelation functions do not match well with the numerical calculations (see Fig. 3.5b). Hence, the number of

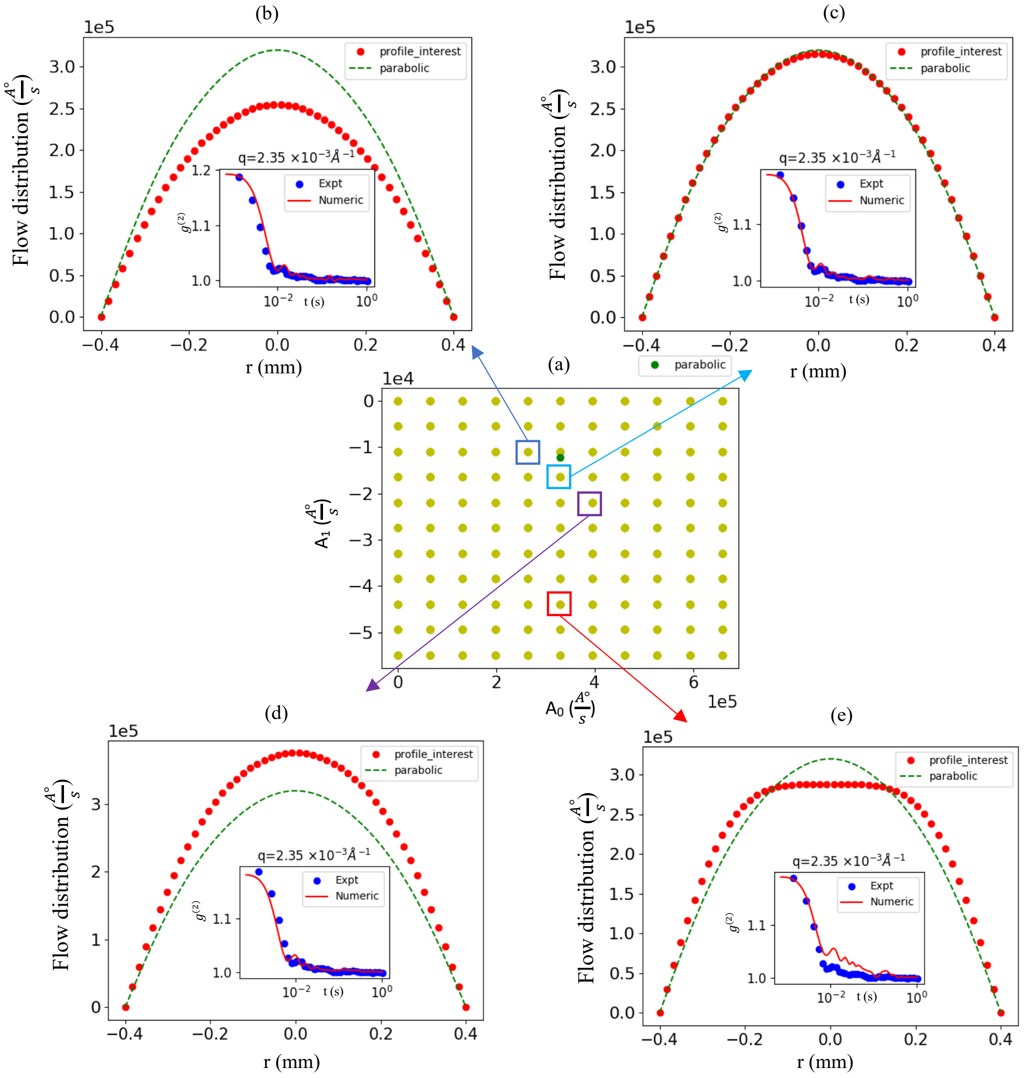

Figure 3.4: (a) Fourier mode phase space representing Fourier modes of parabolic flow profile (green) and grid points (yellow). (b)-(d) Flow profiles (red circles) of the nearest neighbors close to parabolic flow Fourier modes and parabolic flow modes (green dashed lines). Inset plot of the corresponding numeric autocorrelation functions (red) using Eq. 3.9 and experimental correlations (blue) for the region ($\mathbf{q}$,ϕ_0) = $\mathbf{2.35}\times 10^{-3}$ $\mathring{A}^{-1}$, 101°).(e) Flow profile of a node farther from parabolic flow Fourier modes which has a "plug" shaped profile (red circles) and the corresponding experimental (blue) and numeric (red) autocorrelations in the inset.

modes are increased monotonically and the mean square error (MSE) using Eq. 3.10 for each case is calculated. When three modes are used, the fits between the experimental and numeric autocorrelations match very closely and the MSE is significantly reduced (see Fig. 3.5d). It can be seen that the error decreases as the number of modes are increased and the error does not decrease further if more than 3 modes are used as shown in Fig. 3.5e.

Based on this analysis, using three Fourier modes were adopted for the velocity profile decomposition. Therefore, a 3-dimensional matrix is generated around the parabolic flow modes (green point) as shown in Fig. 3.6(1-a). Each coordinate in the mode space represents a unique set of Fourier modes (i.e., $A_0, A_1 \& A_2$). Flow profiles for each coordinate was obtained from the Fourier series summation using Eq. 3.7 to obtain numerical autocorrelations as discussed below.

The intensity fluctuation auto-correlation functions for the second term in Eq. 3.5 (decay due to shear) were calculated numerically which will be referred as $g^{(2)}_{num}$, using the Eq. 3.9 via double summation over all pairs of particles having velocity differences (δv) at prescribed scattering wave vector (q) using

$$|g_1,_S(\mathbf{q},t)|^2 = \frac{1}{4R^2}\int_{-R}^{R}\int_{-R}^{R} cos(\mathbf{q}t\delta v(r_1,r_2))dr_1dr_2 \tag{3.9}$$

where δv = velocity difference between the particles at positions $r_1 \& r_2$ respectively.

The numerical calculations $g^{(2)}_{num}$ were performed for each flow profile in the phase space using the equation above. The objective is to obtain the flow profile which has the smallest MSE between the experimental data; i.e $g^{(2)}_{expt}$ from all the regions in detector and $g^{(2)}_{num}$ for the same regions. In order to achieve this, a grid of coordinates (yellow circles) of volume 21 × 21 × 21 was generated around the parabolic flow modes. The intensity autocorrelation functions were computed numerically for each coordinate; i.e flow profiles in the phase space using the Eq. 3.9. The MSE was calculated between $g^{(2)}_{expt}$ from the experiments and $g^{(2)}_{num}$ via numeric calculations for each profile via Eq. 3.10. Fourier modes corresponding to the flow profile with lowest MSE is shown as the blue square in Fig. 3.6(1-b). The flow profile with the lowest MSE, along with flow profile generated using Fourier modes from parametrization of Poiseuille equation were plotted together as

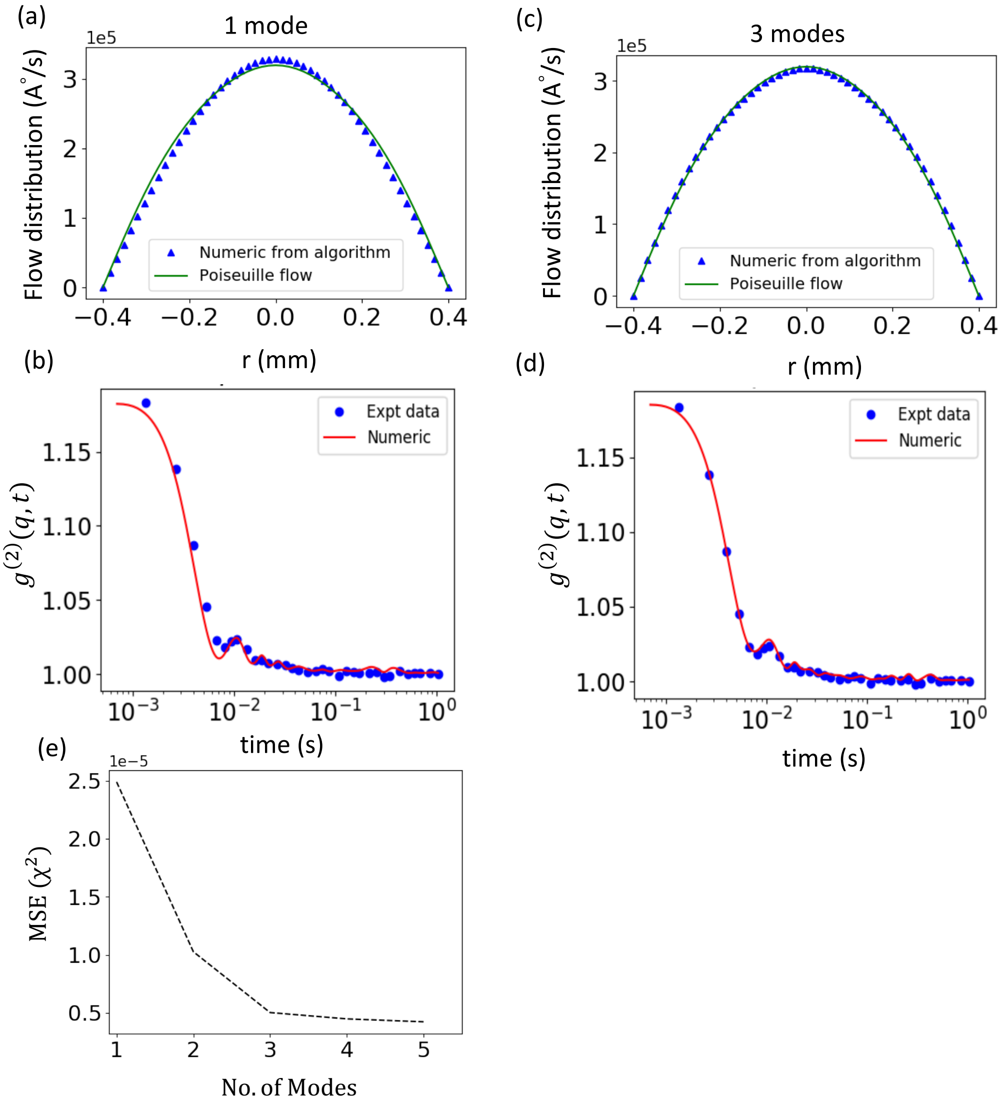

Figure 3.5: Mean Square Error (MSE) variation of the developed technique with number of modes. (a,c) Flow profiles of parabolic Poiseuille flow (green) and profile with lowest MSE from Fourier mode decomposition (blue triangles) for 1 mode & 3 modes phase space respectively. (b,d) Experimental autocorrelations (blue circles) and numeric intensity autocorrelations (red) of the best set of modes from MSE calculations for 1 mode and 3 modes phase space respectively for the region $(\mathbf{q},\phi_0) = \mathbf{2.35}\times10^{-3}\ \AA^{-1}, 101^{\circ})$. (e) MSE with number of Fourier mode(s) phase space.

Figure 3.6: Fourier mode decomposition with 3 modes A_0, A_1 & A_2 respectively. No's 1,2,3 represents iterations. 1(a) 3D map of the decomposed Fourier mode phase space with Fourier modes of parabolic flow profile (green circle) and best set of modes (blue square) from MSE calculations. 1(b) 2D projection of the phase space. 1(c) Numeric fits of intensity autocorrelations of the best set of modes shown in 1(b) and comparison with experimental autocorrelations for the region ($\mathbf{q}$,ϕ_0) = $\mathbf{2.35}\times10^{-3}$ $\AA^{-1}$, 101°). 1(d) Flow profiles of best set of modes (blue triangles)and parabolic flow modes (green) obtained via Eq. 3.7. 2(a) 3D map of the decomposed Fourier mode phase space with parabolic flow modes (green circle) and best set of modes (cyan triangle) in the 2nd iteration. 2(b) 2D projection of the new phase space. Inset plot with best set of modes in 1st (blue square), 2nd (cyan triangle) iterations and parabolic flow modes (green circle). 3(a) 3D map of the decomposed Fourier mode phase space with parabolic flow modes (green circle) and best set of modes (magenta circle) in the 3rd iteration. 3(b) 2D projection of the new phase space. Inset plot with best set of modes in 1st (blue square) ,2nd (cyan triangle), 3rd (magenta circle)iterations and parabolic flow modes (green circle). 2,3 (c) Numeric fits of intensity autocorrelations of the best set of modes and comparison with experimental autocorrelations for respective iterations for the region ($\mathbf{q}$,ϕ_0) = $\mathbf{2.35}\times10^{-3}$ $\AA^{-1}$, 101°). 2,3(d) Flow profiles of best set of modes (cyan triangles & magenta triangles respectively)and parabolic flow modes (green) obtained via Eq. 3.7.

shown in Fig. 3.6(1-d).

$$MSE(\chi^2) = \sum_{i=0}^{N} \left(\frac{g^{(2)}_{expt(i)} - g^{(2)}_{num(i)}}{g^{(2)}_{expt(i)}} \right)^2 \tag{3.10}$$

The MSE calculations can be improved iteratively by generating a new mesh (Fig. 3.6(2-b))around the best set of modes of the previous iteration. The iterative process is repeated and the MSE was computed between $g^{(2)}_{num}$ and $g^{(2)}_{expt}$ for each iteration. The new grid (inset of Fig. 3.6(2-b)) shows that modes from numerical calculations (cyan) in this iteration is closer to the parabolic flow modes (green point). The calculations were further improved by generating a new grid at every iteration from the best set of modes of the previous iteration. This process was repeated for only 6 iterations, after which the MSE is no longer reduce (i.e., by more than 1%).

3.6 Sensitivity to noise-to-signal ratio

In order to test the sensitivity of the developed method to the noise-to-signal ratio, synthetic data with different noise levels was generated using the Eq. 3.11. The synthetic data are the intensity auto-correlations functions that are derived analytically by assuming Hagen-Poiseuille profile configuration plus additional white noise of varying magnitude. Flow profiles were obtained for noise levels 5 to 20%, as shown in Fig. 3.7.

$$\left|g^{(1)}(\mathbf{q},t)\right|^2_{noise} = \left|g^{(1)}(\mathbf{q},t)\right|^2_{syntheticdata} + NA \times \beta \times \text{rand} \tag{3.11}$$

Table 3.1: Mean Square Error (MSE) at different noise levels

Noise levels	MSE	Q_{num}/Q_{sol}
5%	2.65e-5	0.99
10%	9.83e-5	0.99
20%	3.7e-4	0.89

where β is the speckle contrast, rand is random white noise (values between -1 and 1) which has same size as $g^{(2)}_{syntheticdata}$, NA is the noise amplitude.

In the first case(a), synthetic data with **5%** noise was created (green triangles) using the Eq. 3.11. MSE calculations were performed between the experimental correlations and synthetic data with noise. Velocity profile of the best set of Fourier modes with the lowest MSE (blue triangles) were obtained from Fourier mode decomposition and compared against Poiseuille flow distribution (green), there is a good agreement with numeric calculations and velocity profile from the Poiseuille profile. In the second case(b), synthetic data with **10%** noise was created (green triangles) and we repeat the procedure of obtaining velocity profile and compared against Poiseuille flow distribution.There is still a good agreement with numeric and flow profile from Poiseuille profile. In the final case(c), synthetic data with **20%** noise was created (green triangles), there is a deviation from the expected Poiseuille flow profile. Thus the established methodology of obtaining flow profiles from Fourier Mode decomposition is quite robust up to 10% error in the signal (speckle contrast) from the x-ray measurements. The analysis shows that the studied algorithm for finding the optimal set of Fourier modes is able to find an accurate representation of the flow profile for noise-to-signal ratios up to 20% for the studied flow conditions.

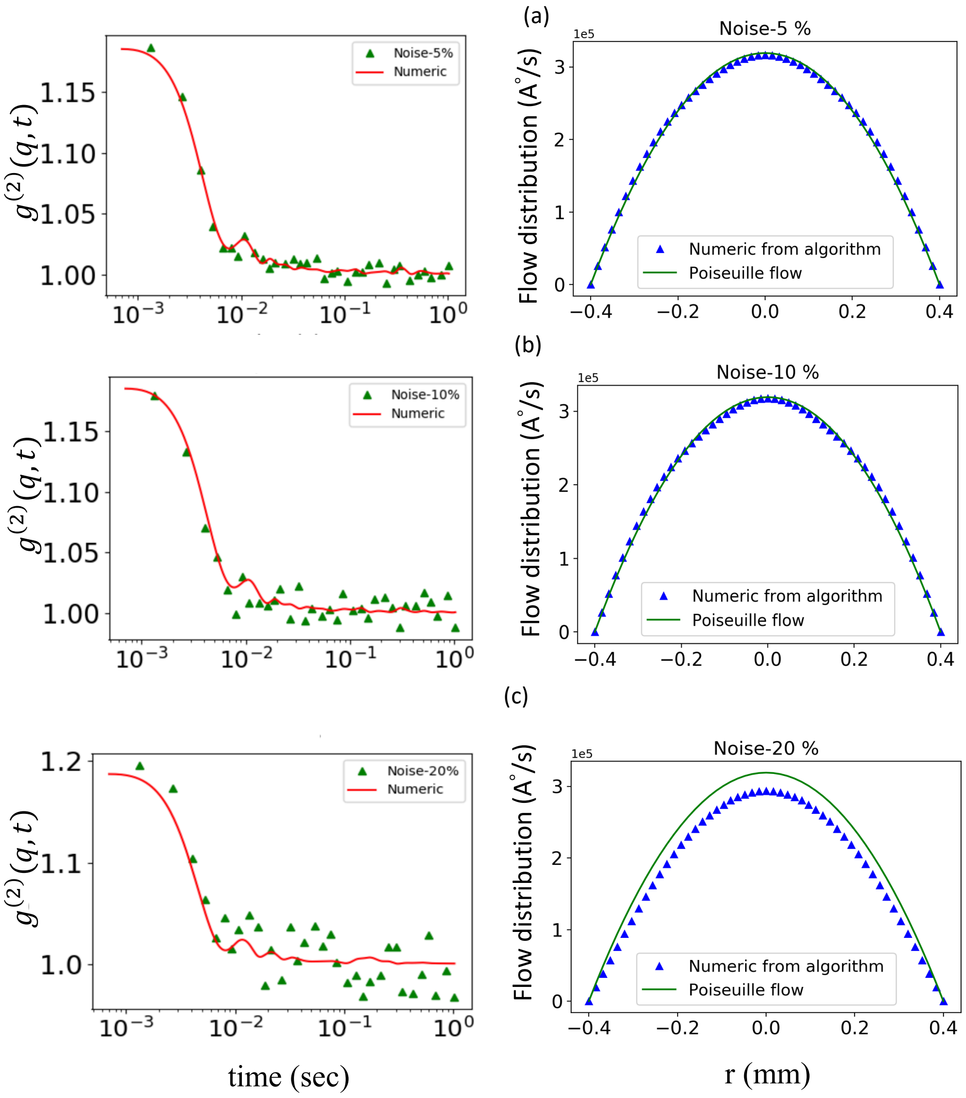

Figure 3.7: Synthetic data at different noise levels. (a-c) Intensity autocorrelations with 5 %,10% & 20% noise (green triangles) and autocorrelation functions from the numeric calculations (red) on the left panel. The corresponding flow profiles (blue triangles) from numeric fit and parabolic Poiseuille flow (green) are shown on the right panel.

Chapter 4

Capillary Diode Devices for Selective Liquid Transport

In this Chapter, I present an experimental and theoretical analysis of the feasibility of employing a capillary deices with diode-like properties for the transport of immiscible liquids such as water and oils [72]. The diode-like properties with asymmetric liquid conductivities in a "forward" and "backward" direction are induced by micro/nanopatterning the device surfaces in order to induce large surface energy barriers and long-lived metastable states. Experiments studying vertical capillary imbibition for water and oil are performed to characterize the analytically predicted diode-like behavior of the fabricated devices and to assess their potential for water-oil separation.

4.1 Theoretical model

The studied capillary device (Fig. 4.1a) consists of a 3D slit channel of length ℓ with a rectangular cross section of width w and narrow height $h \ll w$, that is filled with two immiscible fluids A and B having an interfacial tension $\gamma = \gamma_{AB}$. The slit channel has two sections 1 and 2 having different effective surface energies γ_{A1}, γ_{A2} and γ_{B1}, γ_{B2} when wetted by fluid A and B, respectively. Hence, the surface energy difference $\Delta\gamma_i = \gamma_{Ai} - \gamma_{Bi}$ determines the Young contact angle $\cos\theta_i = -\Delta\gamma_i/\gamma$ for each section $i = 1, 2$. The junction between the two different sections of the slit having lenghts L_1 and L_2, respectively, is located at a distance $z_j = L_1 - d$ measured from the flat interface at

$z = 0$, when the leading edge of the slit is immersed at a depth d (Fig. 4.1a).

This analysis focuses on the case of vertical imbition (Fig. 4.1a) where the capillary diode is in contact with a large bath of fluid A and capillary action, when $\theta_1 \leq \theta_2 < 90°$, drives phase A upward against the action of gravity. As the fluid phase A displaces phase B, the average position of the three-phase contact line $z = (1/\mathcal{S}) \times \int_0^{\mathcal{S}} f(s)ds$ is given by averaging the local contact line position $f(s)$ (Fig. 4.1a) along the full contact line perimeter $s = 0, \mathcal{S} = 2(w + h)$. It is considered that the closed system comprising the capillary slit and the fluid phases A and B is in thermal and chemical equilibrium. Furthermore the fluids A and B are considered to be incompressible with a constant mass density ρ_A and ρ_B, respectively. The system free energy can be parameterized by the average contact line position and thus can be expressed as

$$\mathcal{U}(z) = \frac{1}{2}\Delta\rho g w h z^2 + \gamma w h \frac{(\pi - 2\theta)}{2\cos\theta} + 2\Delta\gamma(z)(w + h)z \tag{4.1}$$

where $\Delta\rho = \rho_A - \rho_B$ is the mass density contrast, g is the gravitational acceleration, θ is the apparent contact angle at the three-phase contact line, and

$$\Delta\gamma(z) = -\gamma\cos\theta_1 + \frac{\gamma}{2}(\cos\theta_1 - \cos\theta_2)\left[1 + \tanh\left(\frac{z - z_j}{\delta}\right)\right] \tag{4.2}$$

is the surface energy difference, which is modeled as having a gradual spatial variation centered at z_j and over a finite distance $\delta = (1/\mathcal{S}) \int_0^{\mathcal{S}} (f(s) - z)^2 ds$. The amplitude of spatial variations $|f(s) - z|$ of the local contact line position is determined by a balance between surface and gravitational energy and thus $\delta = \ell_c g(\theta)$, where $\ell_c = \sqrt{\gamma/\Delta\rho g}$ is the capillary length and $g(\theta) \sim \mathcal{O}(1)$ is a shape factor that is close to unity for $w \gg \ell_c$ and $\theta \ll 1$.

Under the modeled conditions, the effective driving force for the displacement of the average contact line position is $F(z) = -\partial\mathcal{U}/\partial z$. The global minimum of the free energy $\mathcal{U}$ in Eq. 4.1, and thus the stable equilibrium condition, is located at $z_E = (2\gamma\cos\theta_2/\Delta\rho g) \times (1/h + 1/w)$ provided that z_j is sufficiently smaller than z_E. Moreover, Eqs. 4.1–4.2 predict a local energy minimum at the critical value

$$z^* \simeq (\cos\theta_1 + \cos\theta_2) \times \left[\frac{\Delta\rho g}{\gamma(1/h + 1/w)} + \frac{(\cos\theta_1 - \cos\theta_2)}{\delta}\right]^{-1}. \tag{4.3}$$

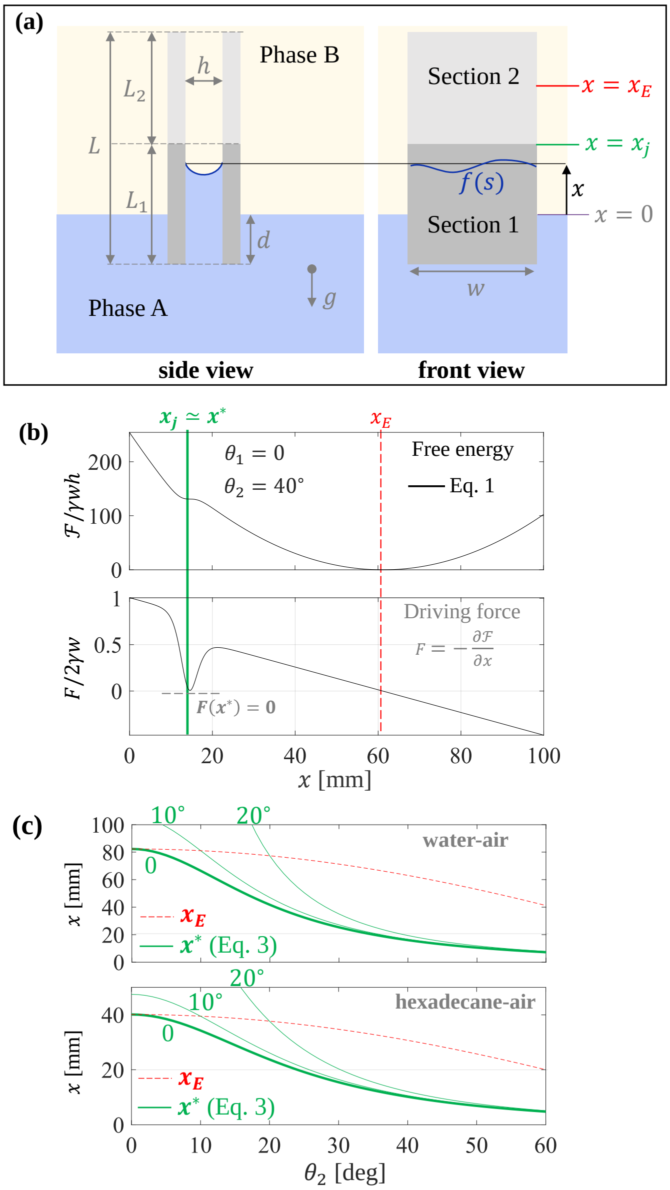

Figure 4.1: Device design and analytical description

As shown in Fig. 4.1b for the particular case of $\theta_1 = 0$ and $\theta_2 = 40°$, when the position of the junction $z_j \geq z^*$ is equal or larger than the critical value defined by Eq. 4.3 the capillary imbibition of liquid will stop at a metastable equilibrium position for which $F(z^*) = 0$ and there will be no conduction of fluid inside the slit beyond that point. The metastable equilibrium at $z = z^* < z_E$ with no fluid conduction will be observed for long observation times, provided that the energy barrier to cross the junction $\Delta\mathcal{U} \simeq 2\gamma|\cos\theta_2 - \cos\theta_1|(w+h)z_j \gg k_B T$ is orders of magnitude larger than the thermal energy $k_B T$ and the assumption of chemical and thermal equilibrium leading to Eq. 4.1 is valid (e.g., when evaporation and surface condensation is not significant).

Analytical predictions from Eq. 4.3 for the critical junction position to produce metastable equilibrium are reported in Fig. 4.1c for the case of water or hexadecane oil in a microscale slit of height $h = 180\ \mu$m and width $w \gg h$ with a liquid-infused and conventional surface for which $\theta_1 \simeq 0$, 10, or 20° and $\theta_2 =$ 20-60°, respectively, and assuming $\delta = \ell_c$ is determined by the capillary length for each liquid pair. Placing the junction position at 20 mm above the flat interface (Fig. 4.1c) will stop the capillary imbibibtion of water when $\theta_1 \lesssim 20°$ and $\theta_2 \geq 35°$, which are equilibrium contact angles within the range commonly observed for water on hydrophilic surfaces such as micropatterned or conventional glass. For same slit geometry and type of surfaces, the equilibrium contact angles of hexadecane or other oils are expected to be significantly lower ($\theta_1 \simeq \theta_2 \leq 20°$) and the capillary conduction of oil will be able continue above the junction until reaching the stable equilibrium state at $z_E > z^*$ or fill the entire slit when $L \leq z_E$.

Analytical predictions from Eq. 4.3 for the particular conditions reported in Fig. 4.1c thus indicate that a simple prototype device with $z_j \simeq 20$ mm can prevent the vertical capillary imbibibition of water into the second section where $z > z_j$, while oil can readily flow over the junction and fill the second section of the slit. Both water or oil can flow over the junction if its position is reduced to $z_j = 10$ mm, which can be readily accomplished by immersing the edge of the device at $d = 10$ mm inside the fluid bath (Fig. 4.1a). This analytical finding suggests a possible strategy for separation of water from a mixture of water and a less dense oil by immersing in the mixture the analyzed capillary device at controlled depths for which only one or both phases can flow continuously through the slit channel. In particular, a device with a first superhydrophilic section filled with water can be potentially employed as a fluidic diode preventing spontaneous or forced imbibition by any liquid below a threshold pressure head $\Delta p^* = \Delta\rho g(z_E - z^*) > 0$ across the slit channel.

4.2 Experimental Methods

A facile fabrication method involving laser ablative patterning was employed by Prof. Hwang's group to produce the studied fluidic capillary device consisting of a microscale slit with two sections having different effective surface energies, and thus different equilibrium contact angles θ_1 and $\theta_2 \lesssim \theta_1$, for different liquid pairs (e.g., water-air, oil-air, and water-oil). The equilibrium contact angles and their hysteresis are experimentally determined by optical goniometry and Wilhelmy plate measurements. The prototype device is designed according to the model presented in Sec. 4.1 to work as capillary diode or check valve with a critical pressure head Δp^*, attained at a critical immersion depth d^* that is significantly different for the case of water and oil in ambient air, which thus enables the selective capillary conduction of these liquids.

4.2.1 Laser-based Fabrication

The fabricated device fabrciated by Prof. Hwang's group consists of a rectangular slit channel with a nominal gap height $h = 180 \pm 5 \mu m$, width w= 25.4 mm, and length L = 50.8 mm (Fig. 4.2a) that is made of two borosilicate glass slides separated by spacers. The fabrication begins with a well established laser ablation process [73–75] on both sides of the two borosilicate glass slides (i.e., inner and outer channel surfaces) to produce a micropatterned surface section of length L_1 = 20 mm as described in Fig. 4.2a.

A picosecond laser (RG10-H, Photonic Industries International Inc.) of 532 nm in wavelength, 12 ps in full width half-maximum temporal pulse width, 100 kHz in the pulse repetition frequency and up to 7W in average laser power, is used for patterning the glass surfaces. The laser beam was focused on the glass surface with an infinity-corrected objective lens of 0.14 in numerical aperture (Plan APO 5X, Mitutoyo) to the laser spot diameter of 10 μm by 1/e definition. The glass surfaces are scanned with a fixed speed of 20 mm/s using precision XY motion stages (LS103H-100- XY, Aerotech Inc.) and a fixed laser power of 400 mW. The laser power is precisely adjusted by an external attenuator set composed of a half waveplate and a polarizing beam splitter. A zoom lens (12× zoom lens system, Navitar Inc.) and a charge-coupled device (CCD) camera (XC-75, SONY) were implemented at the back of the objective lens to precisely locate laser focus on the sample surface and in situ monitor the laser machining process. The surface pattern consists of parallel microgrooves of depth $d_g \simeq 7\mu$m and width $w_g \simeq 10\mu$m that cover the entire slit width with a uniform spacing s = 50 μm . Nanoscale features of small linear dimensions (∼10 to 100 nm) that fully cover the patterned glass surface are deposited during the laser ablation process. The patterned slides are bonded together using spacers and sealed with epoxy to produce a rectangular slit channel open on both ends.

4.3 Surface wetting characterization

The contact angles for the patterned (section 1) and plain (section 2) surfaces of the fabricated slit were determined using the sessile drop and the Wilhelmy plate methods for the case of water and hexadecane oil in ambient air, as reported in Figs. 4.2b-c. For the reported measurements the glass slides were cleaned with DI water and anionic detergent (Alconox) in an ultrasonic bath sonicator, followed by isopropyl alcohol and DI water rinse. Deionized (DI) water and hexadecane stained with Oil Red O for visualization were employed for the measurements in Figs. 4.2b-c. The surface tension measured using the Du Nouy ring method in ambient air before and after the experiments was γ= 72.5 ±5% mN/m for DI water and γ= 28.5 ±5% mN/m for hexadecane; the addition of Oil Red O did not produce noticeable changes in the surface tension measured for the hexadecane oil. For the contact angle measurements with the sessile drop method, a controlled droplet volume V_d= 10 μL was deposited using a pipette on the patterned and plain (non-patterned) surface and the equilibrium contact angle was determined from digital images using the software ImageJ [76], with 8 to 10 repeated measurements to determine average values. For the case of water (Fig. 4.2 b) on the patterned surface (section 1) thin wetting films were formed with low apparent contact angles that we were not able to determine accurately with the employed optical method, while sessile droplets formed with a contact angle $\theta_2 = 41° \pm 9\%$ measured on the plain glass surface (section 2). For the case of hexadecane oil (Fig. 4.2b), while again the formation of thin films with extremely low apparent contact angle on the micropatterned surface precluded an accurate determination of the apparent contact angle, a small but finite contact angle θ_2 $=15° \pm 10\%$was determined on the plain surface. Contact angle values $\theta_1 \simeq 21.4°$ for water and θ_1 =0 for oil on the patterned surface can be analytically estimated with the Wenzel equation $\cos\theta_1 = rcos\theta_2$ using the roughness factor $r = (s + 2d_g + w_g) = (s + w_g)) =$ 1.23 determined by the ratio of the contact area to the projected area for the fabricated microgroove pattern, with the spacing s = 50μm, and the nominal microgroove depth d_g= 7μm and width w_g =10μm.

Further experimental characterization of the contact angle and its static hysteresis on each section of the fabricated slit was performed with the Wilhelmy plate method (Fig. 4.2c) at a low plate speed V = 5 mm/min that corresponds to extremely small capillary numbers Ca $\sim 10^-6$ and "quasi-static"conditions with negligible hydrodynamic effects. Force measurements reported in this work were obtained with a Sigma 700 force tensiometer (Biolin scientific) using as Wilhelmy plates the partially patterned borosilicate slides employed to build the capillary slits. Wilhelmy plate measurements at sufficiently slow plate speeds enable the determination of the static advancing and receding contact angles θ_A and θ_R, respectively, with the advancing contact angle $\theta_A > \theta_B$ observed during the immersion of the plate. Our measurements (Fig. 4.2c) report a negligible contact angle hysteresis $\theta_A - \theta_R \lesssim 5°$ on the micropatterned surface section for both cases of wetting by water and oil in ambient air. As expected, a significant contact angle hysteresis $\theta_A - \theta_R \simeq 35°$ is observed for the case of water wetting the non-patterned surface section. For the case of water in air, the micropattern produces not only a significant reduction of the equilibrium contact angle θ_1 (Fig. 4.2b) but also the suppression of contact angle hysteresis on the first section of the fabricated capillary slit device (Fig. 4.2c). The observed wetting behavior indicates that the micropatterned surface is infused by the wetting liquid (i.e., water or oil), which remains within the slit after multiple successive immersion and withdrawal cycles performed during the Wilhelmy plate measurements. Moreover, analytical predictions for the presence of a metastable state (Fig. 4.2c) preventing imbibition of water remain valid when considering the observed hysteresis range and the measured contact angles $20° \lesssim \theta_2 \lesssim 60°$ on the plain surface and $\theta_2 = 20 \pm 2°$ on the patterned surface section.

4.4 Results and discussion

Here, I present the main results of the experimental study of the fabricated capillary diode and compare the experimental data with predictions from analytical model described in Section 4.1.

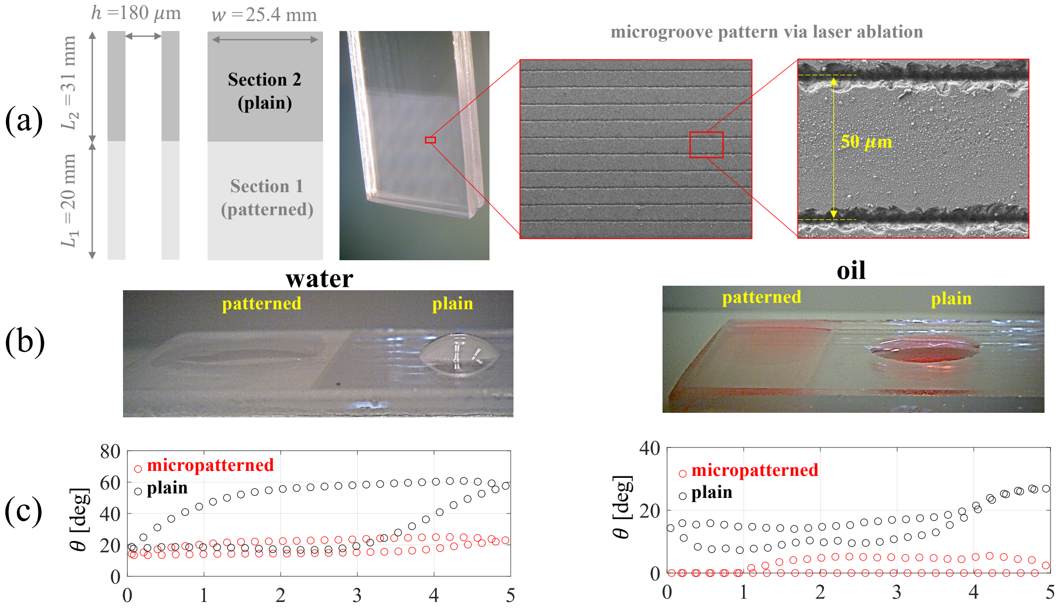

Figure 4.2: Fabricated capillary device and surface wetting behavior. (a) Glass slit (gap height h= 180μm) having a 20-mm long surface section patterned via laser-ablation with microgrooves (SEM images) uniformly separated at distance s=50 μm. (b) Sessile droplet and wetting film formation for water and hexadecane oil observed on the plain (non-patterned) and micropatterned surface sections for water and oil. (c) Contact angle (advancing/receding) hysteresis for water and hexadecane oil on the plain and micropatterned surface sections obtained using the Wilhelmy plate method during immersion/withdrawal.

4.4.1 Vertical imbibition

Based on the equilibrium contact angles determined for water in Sec. 4.3, the studied capillary diode device is designed and fabricated with a micropatterned surface section of length $L_1 =$ 20 mm in order to prevent the imbibition of water in ambient air for a significant range of immersion depths $0 \leq d \leq d^*$, where the critical immersion depth $d^* = L_1 - z^* \simeq 5 - 8$mm is estimated by Eq.4.3 with $\delta / l_c \simeq$0.8-1.1. The estimated critical immersion depth corresponds to a threshold pressure head $\Delta p^* = \Delta \rho g(z_E - z^*) \simeq$0.46-0.5 kPa for vertical imbibition of water. In the case of hexadecane oil for which $\theta_1 \simeq \theta_2$, Eq. 4.3 gives $d^* \simeq 0$ and the fabricated device is expected to behave as a conventional capillary slit at any immersion depth.

Vertical imbibition experiments with DI water or hexadecane oil in ambient air (Fig. 4.3) are performed by immersing at precisely controlled depths d the fabricated capillary device with a micropatterned section and a conventional capillary slit with the same nominal dimensions. The experimental setup employed is illustrated in Fig. 4.3a, the capillary slit is hooked to the force tensiometer with a motorized stage to lift and lower the liquid bath (positioning resolution 0.016 μm) that enables the automatic and precise detection of the flat bath interface (z = 0) and control of the immersion depth d. The tensiometer force is zeroed at the beginning of the experiment when the studied sample and clamp arrangement is outside the liquid bath (Fig. 4.3a). The liquid bath is then lifted slowly at a slow constant speed V = 5 mm/min until reaching the desired immersion depths d = 0 to 16 mm, after which the tensiometer force F(t) is automatically recorded over time at sampling intervals $\Delta t \simeq$0.1 s. The slit remains statically immersed at a depth d for a time interval T after which it is removed outside the bath, completing a full immersion-emersion cycle at the final time t_F(Fig. 4.3 a). The imbibed liquid mass $m(t) = F(t)/g$and the retained liquid mass $m_F = F(t_F)/g$ after removal from the bath are thus determined from the measured tensiometer force, and thus includes a very small additional contribution from the liquid film wetting the outer surfaces of the slit.

As expected for the case of zero immersion depth d=0 (Fig.4.3b-c) and after a short initial time, the imbibed mass rate dm/dt for water ($\rho_A =$ 997 kg/m3) or hexadecane oil ($\rho_A =$ 770 kg/m3) follows the conventional Lucas-Washburn (L-W) prediction [53, 77–79]

$$\frac{dm}{dt} = \rho_A wh \frac{dz}{dt} = \frac{-\rho_A h^2}{12\mu z}\frac{dF}{dz} \tag{4.4}$$

determined from the L-W equation $z - z_E log(1 - z/ z_E) = (\Delta\rho g h^2/12\mu) \times t$, which neglects inertial effects and considers that plane Poiseuille flow develops inside the capillary slit. For the fabricated capillary device with the micropatterned surface section, the water imbibition rate decays sharply after the water-air meniscus reaches the section junction at $z(t) = z_j$, as shown in Fig.4.3b. The observed decay in the imbibed water mass rate is attributed to pinning forces caused by the steep change of the effective surface energy $\Delta\gamma$ near the end of the micropatterned section, as analytically predicted by Eqs. 4.1 , 4.2. This pinning effect is not observed for the imbibition of oil (Fig.4.3c), for which the estimated change in surface energies is less significant between the micropatterned and plain slit sections. To quantitatively compare the water mass retained by a conventional capillary slit and the micropatterned device when immersed at depth d = 0, 4, 8, 12, and 16 mm over a finite time T = 10, 30, and 60 s, we report in Figs. 4.3 (d-e) the mass increase $\Delta M(d,T) = m(t_F) - m_{ref}$, where the reference mass is $m_{ref} =$ M(0,10s) for the conventional capillary slit and $m_{ref} = \rho_A wh L_1$ for the studied device, which corresponds to the water mass to fill the micropatterned section of the studied device. The experimental measurements reported in Figs.4.3 (d-e) correspond to averages over 3 to 5 realizations of immersion-emersion cycles under the same experimental condition, with error bars indicating 90% confidence intervals. For the case of a conventional capillary slit (Fig.4.3d) and sufficiently long immersion times $T \geq 10$ s we observe an expected nearly linear increase of the retained mass$\Delta M \simeq \rho_A whd$ that is caused by increasing the immersion depth. In contrast, the designed capillary device (Fig.4.3d) fills up to the edge of the micropatterned section in less than 10 sec and prevents the further conduction of water above the section junction at $z_j = L_1 - d$ until the immersion depth reaches a critical value $d^* \simeq$ 6mm. The observed critical immersion depth for forward conduction of water in the micropatterned device falls within the analytical estimates for d^* obtained via Eq.4.3(shaded region in Fig.4.3e). The retained mass increase $\Delta M$and effective mass adsorption rate $M \doteq \Delta M/\Delta T$ can be accounted for by a model analogous a simple piecewise linear model for diode behavior [80, 81], with a "turn on" immersion depth d^* and effective forward "conductance " $\Delta M\dot{/}\Delta d = \rho_A wh/\Delta T$ for $d \geq d^*$ in the case of sufficiently long immersion times $T > 10$ s.

In addition to the quantitative analysis in Fig.4.3 direct visualization is reported in the image sequences in Fig.4.4 and Videos S1-S3 in the Supplementary Information (SI). Video imaging confirms that the rising water-air meniscus remains static at the edge of the micropatterned slit section when the leading edge of the device is immersed at d = 4 mm into the water bath (Fig.4.4a and Video S1). As expected, the water phase is able to cross the junction and flow into the second section when increasing the immersion depth to d = 16 mm (Fig.4.4b and Video S2 in SI), which is larger than the predicted critical immersion depth. In contrast, for the vertical imbibition of hexadecane oil, the oil phase is always able to cross the junction at $z_j = L_1 - d$ for $d \geq 0$ and flow into the second section, as reported in Fig.4.4c (Video S3 in SI). Given that the diode-like behavior for the imbibition of water for different immersion depths does not occur for the imbibition of hexadecane oil, the micropatterned capillary device can be employed to selectively adsorb water and oil by controlling the immersion depth d. This suggests the possible application of the studied device for the separation of water and oil through properly devised strategies, as discussed in the next section.

4.4.2 Water-oil separation

In this section we assess the potential for water-oil separation of the studied micropatterned capillary device displaying diode-like behavior in the case of water imbibition (Figs.4.3- 4.4). For this purpose, vertical imbibition experiments were performed as illustrated in Figs.4.5- 4.7 with the studied capillary diode device immersed in a water bath with different deposited volumes of hexadecane oil (1 to 5 mL), which produces oil droplets of diameter (∼20 mm) comparable the slit width or continuous films with a characteristic thickness ∼2 to 3 mm. In all studied cases, immersion speeds (V = 5 - 20 mm/min) lower than the capillary imbibition speeds (1-10 mm/s) predicted by Eq.4.4 for z$\leq z_j$ are employed to ensure the validity of the theoretical analysis and the observation of a metastable state preventing further imbibition at z = z^* (Eq. 4.3). For higher immersion speeds approaching the capillary imbibition speeds, dynamic effects could force the liquid to flow over the position where metastable state is predicted by Eq. 4.3.

The studied device is first in a "dry" configuration (Fig.4.5) where the micropatterned

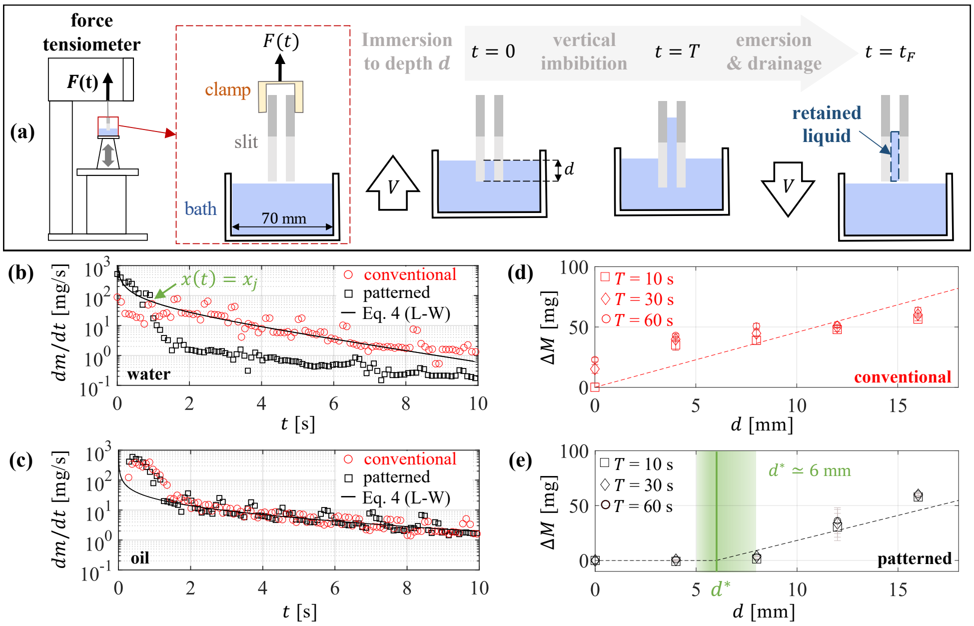

Figure 4.3: Vertical imbibition and adsorption of water and oil. (a) Experimental setup for vertical imbibition experiments with immersion at controlled depths d during a time T followed by removal from the liquid bath. The immersion/withdrawal speed is V = 5 mm/min in all cases. (b)-(c): Instantaneous mass rate dm/dt at d = 0 for water and hexadecane oil in a conventional capillary slit and the fabricated micropatterned device. (d)-(e): Retained water mass increase $\Delta M = m(t_F) - m_{ref}$ (see definition in the main text) in the conventional capillary slit and micropatterned device after immersion times T = 10, 30, and 60 s at immersion depths d = 0, 4, 8, 12, and 16 mm. The critical immersion depth d^*= 6 mm determined from experimental measurements is predicted by Eq. 4.3 for $\delta = l_c$. The shaded region in panel (e) shows a range of analytical predictions for d^* using $\delta / l_c \simeq$0.8-1.1.

(a) Water-air: immersion depth d = 4 mm ($d < d^*$)

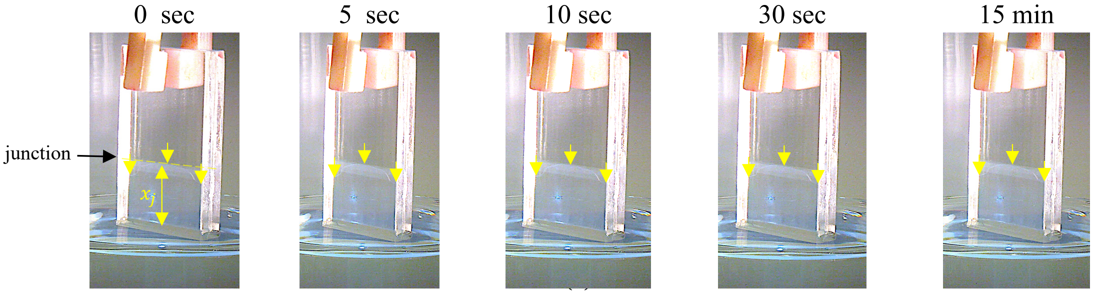

(b) Water-air: immersion depth d = 16 mm ($d > d^*$)

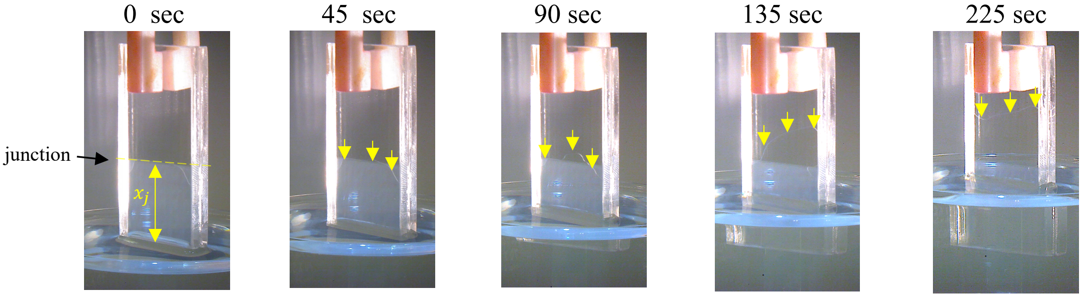

(c) Hexadecane-air: zero immersion depth (d = 0)

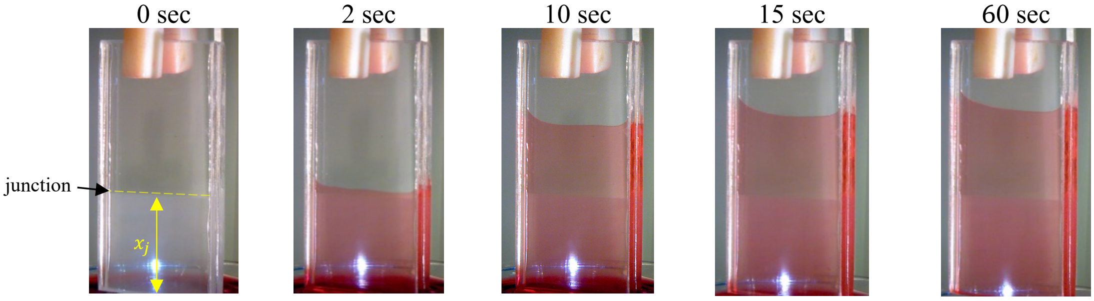

Figure 4.4: Vertical imbibition of the micropatterned capillary device at immersion depths above/below the critical immersion depth mm $d^* \simeq$ 6mm(plate speed V = 5 mm/min). Image sequences are snapshots at different time instances ($t \geq 0$) of Videos S1-S3 in the Supplementary Information. The position z_j of the junction between the micropatterned and bare surface section is indicated by the dashed (yellow) lines. Vertical (yellow) arrows are included to aid visualization of the water-air interface position. (a) Water-air imbibition for $d < d^*$ [Video S1]. The water-air interface is not able to cross the section junction during an observation period of 1 min of static immersion at $d = 4$ mm. (b) Water-air imbibition for $d > d^*$ [Video S1]. The water-air interface crosses the section junction when $z_j \simeq L_1 - d^*$ (t = 90 s), before reaching the targeted immersion depth $d = 16$ mm. (c) Hexadecane-air system at zero immersion depth d= 0 [Video S3]. The hexadecane oil is stained with Oil Red O for visualization. The oil phase crosses the section junction at z_j for any immersion depth d

slit section is empty of any liquid, and a "wet" configuration (Figs.4.6- 4.7) where water fills entirely the micropatterned section, which produces the reported diode-like behavior with a critical immersion depth $d^* \simeq 6$ mm for "forward" liquid conduction. The studied device in dry and wet configurations is immersed in the water bath with hexadecane oil (stained with Oil Red O for visualization) at a slow speed V = 20 mm/min until reaching different immersion depths $d < d^* = 4$ mm and $d > d^* = 16$ mm above and below the critical immersion depth for water imbibition.

As reported in the image sequences in Fig. 4.5, the slit in the "dry" configuration adsorbs both water and droplets of hexadecane oil when the immersion depth is $d < d^*$ (Fig. 4.5b) or $d > d^*$ (Fig. 4.5c), for which both oil and water phases crossing the junction. Hence, the dry-slit configuration leads to the combined imbibition of water and oil and does not produce the effective separation of the liquid phases.

On the other hand, the imbibition cases using a "wet" configuration for which the micropatterned section of the slit is infused with water prior to immersion, result in the selective adsorption of water alone as shown in Figs. 4.6-4.7. Notably, only water is adsorbed within the slit and the oil is not able to flow into the slit for neither the case of droplets smaller than the slit width (Fig. 4.6) or continuous oil films (Figs. 4.7) with a thickness smaller than the critical immersion depth $d^* \simeq 6$ mm. For immersion depths $d < d^*$ smaller than the critical value (see Fig. 4.6b & 4.7b), the water-air interface remains "pinned" at the junction between the patterned and plain section, as previously observed for water-air systems. For sufficiently large immersion depths $d > d^*$, the water phase alone is able to cross the junction flow into the second non-patterned section and fill the slit (see Fig. 4.6c& 4.7c). Hence, immersing the studied device pre-filled with water (i.e., "wet" configuration), the water phase can be effectively separated from the oil through its selective adsorption.

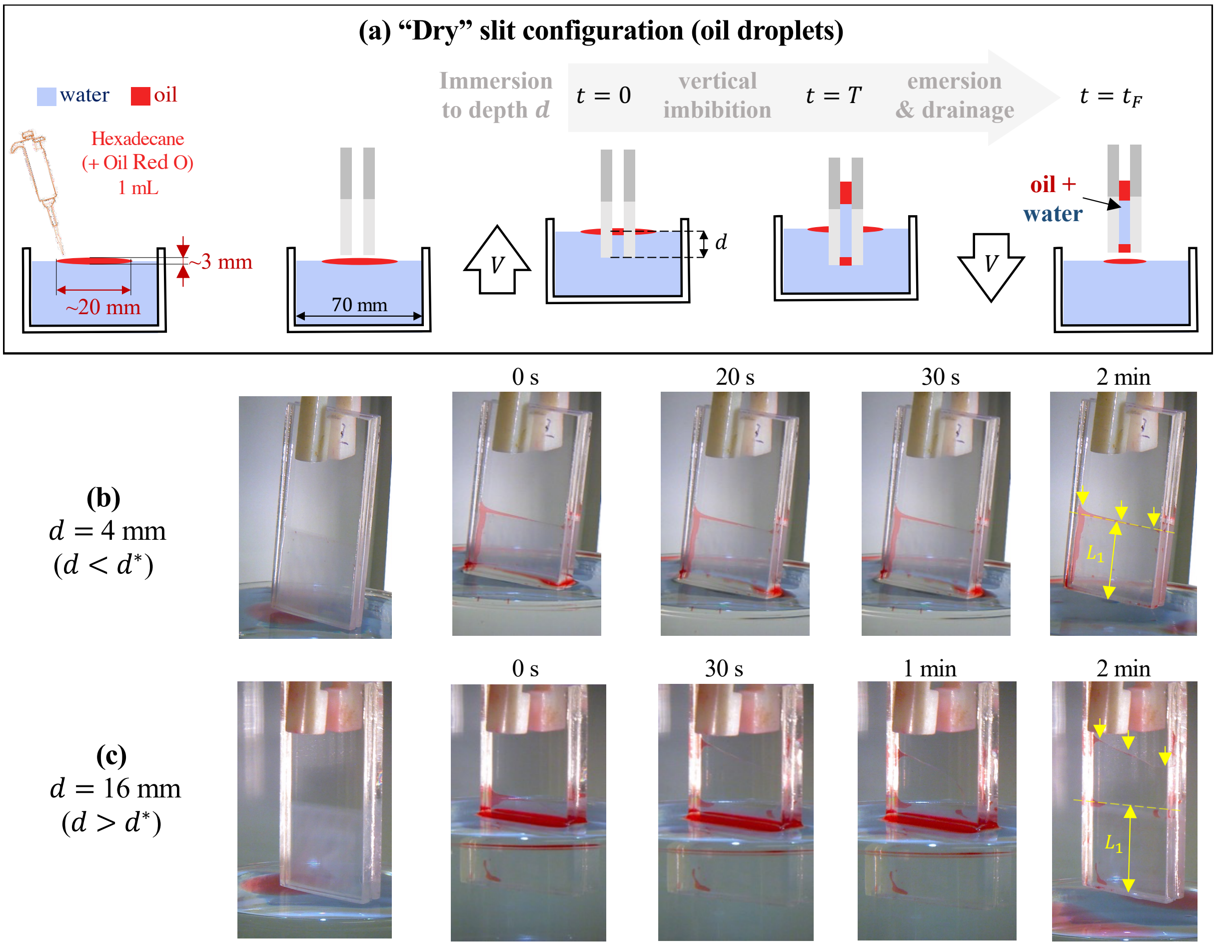

Figure 4.5: Oil-water imbibition behavior in ”dry” device configuration. (a) Dry slit configuration where the micropatterned device does not contain liquid at the beginning of the immersionemersion cycle at controlled depths d. The plate speed is V $=$ 20 mm/min in all cases. An oil droplet of diameter $\simeq$ 20mm and thickness $\sim$ 3mm is deposited on the water-air interface by drop casting 1 mL of hexadecane oil (stained with Oil Red O for visualization). (b) Immersion at depth $d < d^*$smaller than critical ($d=$ 4 mm). The image sequence (Video S4 in SI) shows that both water and oil are adsorbed inside the slit within the micropatterned section. (c) Immersion at depth $d > d^*$ larger than critical ($d=$ 16 mm) The image sequence (Video S5 in SI) shows that both water and oil are adsorbed inside the slit above and below the junction between the micropatterned and plain section. Yellow arrows are visual aids to indicate the position of the water-air interface.

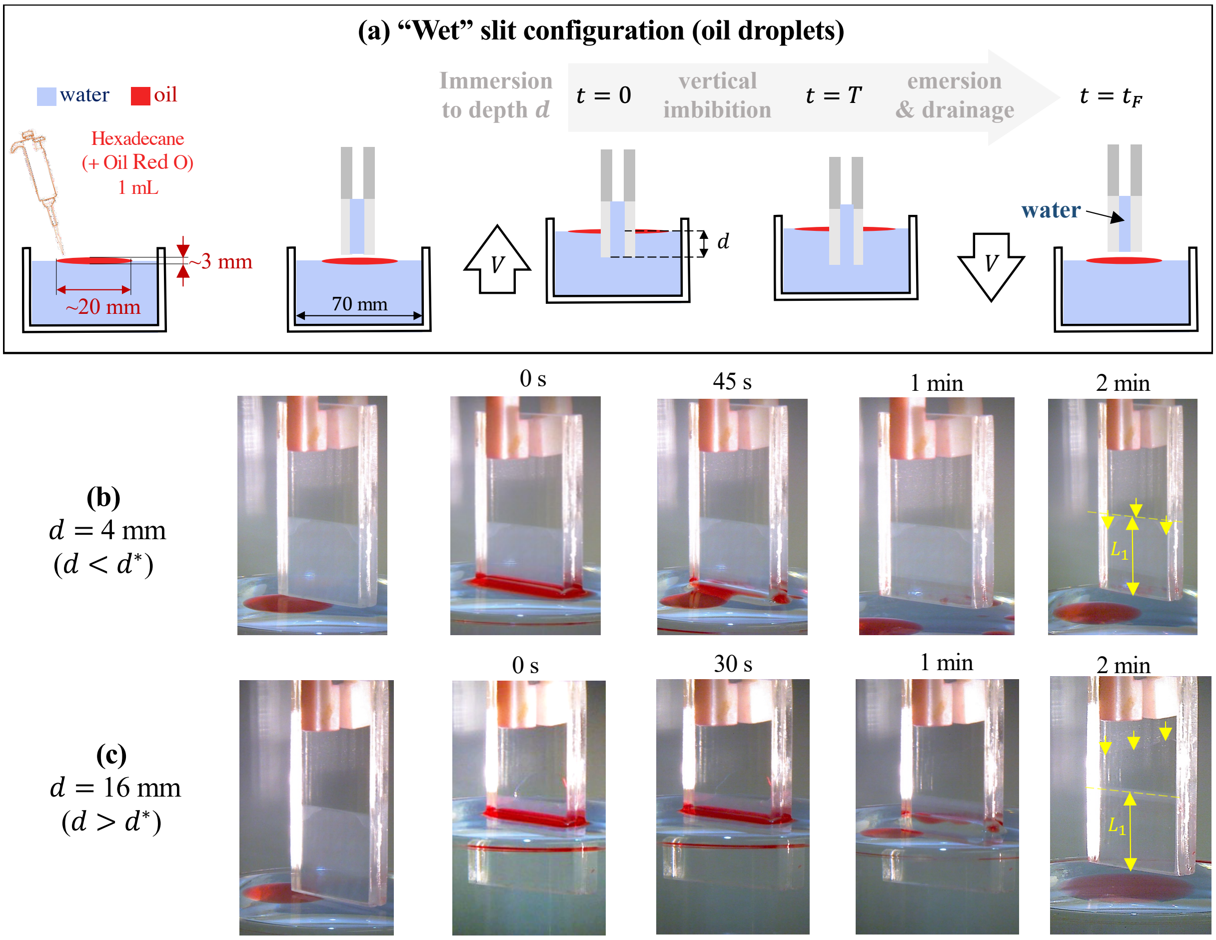

Figure 4.6: Oil-water imbibition and separation in "wet" device configuration. (a)Wet slit configuration where the micropatterned device contains water within the micropatterned section at the beginning of the immersion-emersion cycle at controlled depths d. The plate speed is V = 20 mm/min in all cases. An oil droplet of diameter ~20 mm and thickness ~3 mm is deposited on the water-air interface (hexadecane oil stained with Oil Red O for visualization). (b) Immersion at depth $d < d^*$ smaller than critical (d= 4 mm). The image sequence (Video S6 in SI) shows that only water is adsorbed inside the slit and within the micropatterned section only. (c) Immersion at depth $d > d^*$ larger than critical (d= 16 mm) The image sequence (Video S7 in SI) shows that only water is adsorbed inside the slit both above and below the junction between the micropatterned and plain section. Yellow arrows are visual aids to indicate the position of the water-air interface.

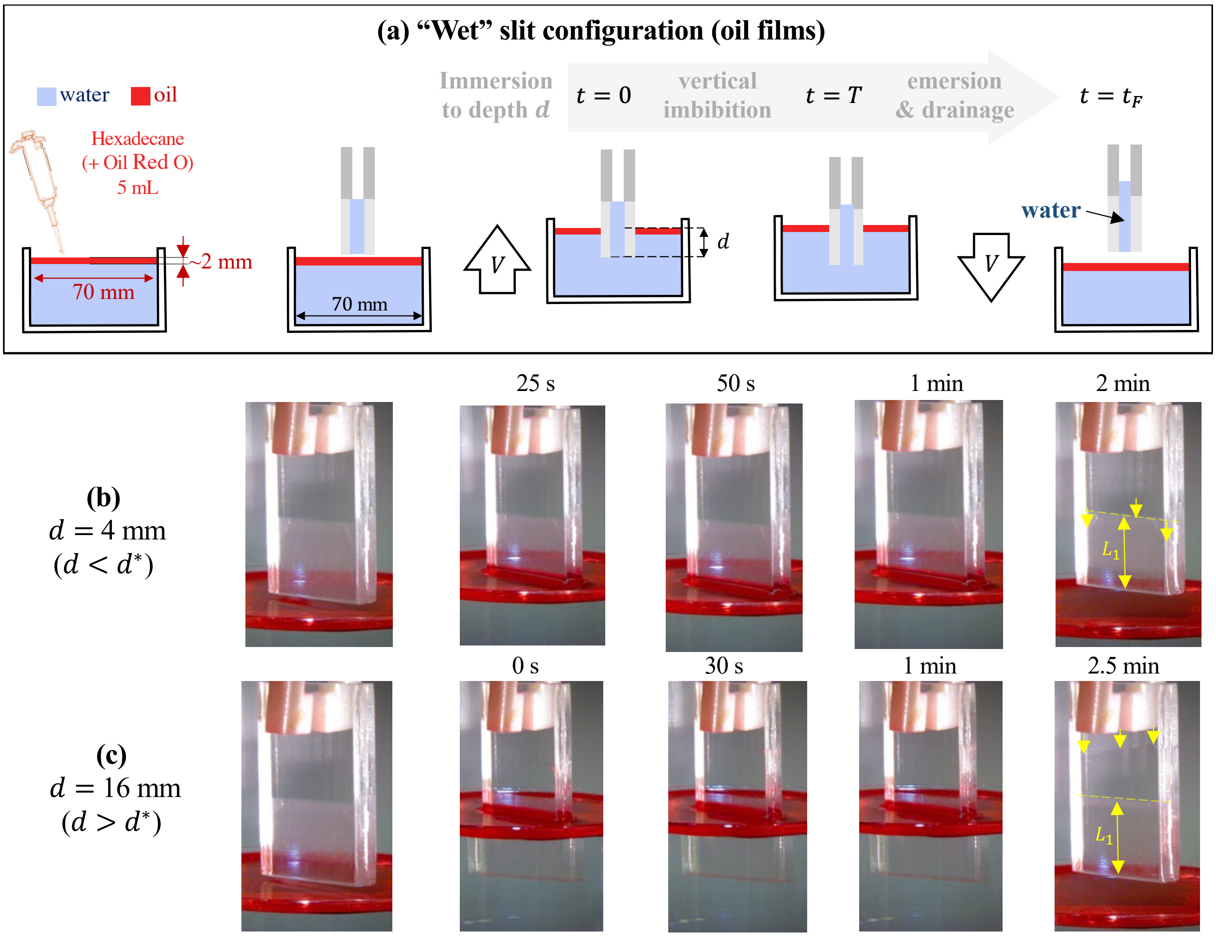

Figure 4.7: Oil-water imbibition and separation in "wet" device configuration (oil films on water). (a) Wet slit configuration where the micropatterned device contains water within the micropatterned section at the beginning of the immersion-emersion cycle at controlled depths d. The plate speed is V = 20 mm/min in all cases. An oil film of thickness ∼3 mm is deposited on the water-air interface (hexadecane oil stained with Oil Red O for visualization). (b) Immersion at depths $d < d^*$ smaller than critical (d= 4 mm). The image sequence (Video S8 in SI) shows that only water is adsorbed inside the slit and within the micropatterned section only. (c) Immersion at depths $d > d^*$ smaller than critical (d= 16 mm) The image sequence (Video S9 in SI) shows that only water is adsorbed inside the slit above and below the junction between the micropatterned and plain section. Yellow arrows are visual aids to indicate the position of the water-air interface.

Chapter 5

Conclusions and Future work

5.1 Characterization of liquid transport in capillaries via XPCS

For the project described in Chapter 3, I developed analysis tools with which spectroscopy analysis using the XPCS method can determine flow velocity profiles of liquids with colloidal nanoparticles that are forced to flow under controlled conditions in capillary channels of know dimensions. In particular, the work focused on developing a “model-free” reconstruction of arbitrary flow profiles using Fourier mode decomposition to represent the flow velocity. A numerical algorithm was developed to find the set of Fourier modes that minimizes the error between the intensity autocorrelation function numerically computed and obtained from experiments. Results using the developed method for a Newtonian liquid give a good agreement with the expected solution for the case of Poiseuille flow with no slip boundary conditions, which can be accurately represented using a small number Fourier modes (e.g., two to four modes or fitting parameters). The solution found is unique when the volumetric flow rate is prescribed. The developed method is suitable for studying the hydrodynamics and rheology of complex liquids and colloidal dispersions using synchrotron-based x-ray spectroscopy methods.

The developed method continues to be tested and further developed in the CHX beamline of NSLS-II. Future work building on this project can use genetic algorithms and more involved machine learning techniques for multiparameter optimization as a more efficient alternative to determine a large number of Fourier modes, which will enable the characterization of complex flow profiles produced by non-Newtonian liquids with complex rheological properties. Better optimization algorithms can very efficiently determine a large number of Fourier modes (e.g., over 100 modes) that would be needed to correctly represent characterize these type of flows near solid-liquid interfaces in the presence of sharp velocity gradients. The developed method has the potential to be employed for studying fluid flows over micro/nanopatterned surfaces given that high spatial and temporal resolution can be attained through further improvements of the numerical algorithm and experimental setup.

Overall, this doctoral work has laid the basis for the development of novel capabilities for the analysis of flowing matter using x-ray spectroscopy in the NSLS-II. Continuing the work in this direction could be greatly beneficial for a large number of researchers from industry and academia that employ x-ray based synchrotron techniques.

5.2 Passive separation in capillary devices

For the second project in this dissertation work, I studied the feasibility of preventing the transport of certain liquid pairs in a capillary conduct by partially micro/nanopatterning the surface of the capillary. A capillary device was designed based on a simple theoretical model and fabricated in glass using a single-step laser-based ablation process by Prof. Hwang's group. The studied device can work as a fluidic diode with vanishingly small hydrodynamic conductance for capillary imbibition of water within a finite range of immersion depths in vertical imbibition. This diode-like effect was attained through patterning a section of predefined length on the device surfaces without resorting to chemical treatment of the hydrophilic glass substrate. While the studied device works as a fluidic diode for water, it behaves as a conventional capillary slit for the imbibition of oils (e.g., alkanes, silicone oils) with low surface tension. A prototype device with simple geometric design demonstrated selective adsorption and separation of water and oil in vertical imbibition experiments at controlled immersion depths.

For the theoretical and experimental analysis of the so-called capillary diodes, I have studied experimentally a simple prototype capillary device consisting of a microscale slit channel with two sections having different surface energies when wetted by different liquid pairs. The contrast in surface energies, characterized by the apparent or effective contact angle was produced by laser-based physical micropatterning a section of the slit channel surface, which under the studied conditions produced a water infused surface occupying a section of predetermined length, and a junction with a conventional non-patterned surface at a specific position z_j measured from the slit channel entrance. The analytical model employed in this work can be used to design the slit channel dimensions and the length of the micro/nanopatterned section infused by water or other liquids in order to induce a metastable equilibrium state, at which the net force driving the conduction of two immiscible fluids becomes vanishingly small for a certain range of pressure heads across the device. The studied device can thus act in manner analogous to a capillary diode with asymmetric capillary conduction of liquid in the forward (imbibition) and backward (drainage) directions. This so-called capillary diode device permits the conduction of liquid water or oil in the “forward” direction ($z > 0$) above different critical values of the pressure head, which results in their selective adsorption under proper conditions.

The theoretical model and experimental results produced in this dissertation work can be employed to improve the design and build new devices for passive separation of water and oil, or to operate as valves or actuators in microfluidic systems. Such fludic devices could be designed based on the demonstrated physical mechanisms and employing the analytical model for considering the effects of micro/nanostructured surfaces that was introduced as part of this dissertation work. The findings in this doctoral work have also reveal the non-trivial effects of nanomaterials (e.g., nano-debris, nanoparticles) deposited during the laser-ablation process for the formation of the micropattern. An interesting area for future work is to employ the analytical tools and experimental protocols developed in this dissertation to design and study fluidic devices having complex micro-patterns and different degree of coverage by nanomaterial in order to control transport properties in microchannels, capillary conducts, and pores.

The properties of the studied device can be exploited for the separation of water and oils and other immiscible fluid pairs having a contrast in their surface energies, that can be amplified by the physical micropattern and/or chemical treatment. A strategy for passive separation of water and oil in vertical imbibition was demonstrated using a simple device produced by a facile fabrication procedure involving laser ablation for the physical micropatterning of glass surfaces. For the case of water in ambient air, the employed surface micropattern with uniformly spaced straight microgrooves produced sufficient surface energy contrast to observe diode-like behavior in vertical capillary imbibition and drainage.

According to the analytical model employed in this work, it is feasible to attain diode-like behavior and enhanced conduction selectivity for different liquid pairs (e.g., water, fuels and oils) by employing alternative surface patterns with more complex geometries and nanoscale dimensions, and additional chemical treatment of the surface using hydrophobic and/or oleophobic coatings. The separation efficiency could be significantly improved by reducing the height of the capillary slit, which prescribes the minimum diameter of oil droplets that can flow into the device when the micro/nanopatterned section is infused with water. Another aspect to be studied is the use of more a complex micropattern geometry in order to increase the perimeter of the junction where the contact line is pinned, which can result in higher critical pressures Δp^* for forward conduction. Future experimental analysis is required to further verify the analytical predictions and assess the performance of prototype devices for concrete technical applications. The planned experiments aim to determine whether sufficiently small oil droplets (i.e., smaller than the slit channel height) are able to enter the capillary slit or remain separated from the imbibing water phase.

Bibliography

[1] R. A. Grubel G., Madsen A., *X-Ray Photon Correlation Spectroscopy (XPCS).* Soft Matter Characterization. Springer, Dordrecht, 2008.

[2] J. D. Smith, R. Dhiman, S. Anand, E. Reza-Garduno, R. E. Cohen, G. H. McKinley, and K. K. Varanasi, "Droplet mobility on lubricant-impregnated surfaces," *Soft Matter*, vol. 9, no. 6, pp. 1772–1780, 2013.

[3] A. Fluerasu, P. Kwasniewski, C. Caronna, F. Destremaut, J.-B. Salmon, and A. Madsen, "Dynamics and rheology under continuous shear flow studied by x-ray photon correlation spectroscopy," *New Journal of Physics*, vol. 12, no. 3, p. 035023, 2010.

[4] G. Fuller, J. Rallison, R. Schmidt, and L. Leal, "The measurement of velocity gradients in laminar flow by homodyne light-scattering spectroscopy," *Journal of Fluid Mechanics*, vol. 100, no. 3, pp. 555–575, 1980.

[5] J. Möller, M. Sprung, A. Madsen, and C. Gutt, "X-ray photon correlation spectroscopy of protein dynamics at nearly diffraction-limited storage rings," *IUCrJ*, vol. 6, no. 5, 2019.

[6] G. Grübel, A. Madsen, and A. Robert, "X-ray photon correlation spectroscopy," 2008.

[7] D. C. Tretheway and C. D. Meinhart, "Apparent fluid slip at hydrophobic microchannel walls," *Physics of fluids*, vol. 14, no. 3, pp. L9–L12, 2002.

[8] S. Busch, T. H. Jensen, Y. Chushkin, and A. Fluerasu, "Dynamics in shear flow studied by x-ray photon correlation spectroscopy," *The European Physical Journal E*, vol. 26, no. 1, pp. 55–62, 2008.

[9] J. Lhermitte, "Using coherent xrays to measure velocity profiles," 2015.

[10] R. Urbani, F. Westermeier, B. Banusch, M. Sprung, and T. Pfohl, "Brownian and advective dynamics in microflow studied by coherent x-ray scattering experiments," *Journal of synchrotron radiation*, vol. 23, no. 6, pp. 1401–1408, 2016.

[11] A. Fluerasu, A. Moussaïd, P. Falus, H. Gleyzolle, and A. Madsen, "X-ray photon correlation spectroscopy under flow," *Journal of synchrotron radiation*, vol. 15, no. 4, pp. 378–384, 2008.

[12] C. Huh and S. Mason, "Effects of surface roughness on wetting (theoretical)," *Journal of colloid and interface science*, vol. 60, no. 1, pp. 11–38, 1977.

[13] J. Oliver, C. Huh, and S. Mason, "An experimental study of some effects of solid surface roughness on wetting," *Colloids and surfaces*, vol. 1, no. 1, pp. 79–104, 1980.

[14] D. Quéré, "Wetting and roughness," *Annu. Rev. Mater. Res.*, vol. 38, pp. 71–99, 2008.

[15] M. E. Kavousanakis, C. E. Colosqui, I. G. Kevrekidis, and A. G. Papathanasiou, "Mechanisms of wetting transitions on patterned surfaces: continuum and mesoscopic analysis," *Soft Matter*, vol. 8, no. 30, pp. 7928–7936, 2012.

[16] M. E. Kavousanakis, C. E. Colosqui, and A. G. Papathanasiou, "Engineering the geometry of stripe-patterned surfaces toward efficient wettability switching," *Colloids and Surfaces A: Physicochemical and Engineering Aspects*, vol. 436, no. 0, pp. 309 – 317, 2013.

[17] C. Colosqui, "Thermodynamics, dynamics, and kinetics at liquid–fluid and fluid–solid interfaces," *Encyclopedia of Interfacial Chemistry*, pp. 654–667, 2018.

[18] R. N. Wenzel, "Resistance of solid surfaces to wetting by water," *Industrial & Engineering Chemistry*, vol. 28, no. 8, pp. 988–994, 1936.

[19] A. Cassie and S. Baxter, "Wettability of porous surfaces," *Transactions of the Faraday society*, vol. 40, pp. 546–551, 1944.

[20] D. M. Kaz, R. McGorty, M. Mani, M. P. Brenner, and V. N. Manoharan, "Physical ageing of the contact line on colloidal particles at liquid interfaces," *Nature materials*, vol. 11, no. 2, pp. 138–142, 2012.

[21] C. E. Colosqui, T. Teng, and A. M. Rahmani, "Wetting driven by thermal fluctuations on terraced nanostructures," *Physical review letters*, vol. 115, no. 15, p. 154504, 2015.

[22] B. M. Jose, D. Nandyala, T. Cubaud, and C. E. Colosqui, "Physical ageing of spreading droplets in a viscous ambient phase," *Scientific reports*, vol. 8, no. 1, pp. 1–8, 2018.

[23] C. E. Colosqui, J. F. Morris, and J. Koplik, "Colloidal adsorption at fluid interfaces: regime crossover from fast relaxation to physical aging," *Physical review letters*, vol. 111, no. 2, p. 028302, 2013.

[24] C. E. Colosqui, J. S. Wexler, Y. Liu, and H. A. Stone, "Crossover from shear-driven to thermally activated drainage of liquid-infused microscale capillaries," *Physical Review Fluids*, vol. 1, no. 6, p. 064101, 2016.

[25] C. E. Colosqui, "Diffusion in a rough potential: Dual-scale structure and regime crossovers," *The Journal of Chemical Physics*, vol. 150, no. 18, 2019.

[26] L. Feng, S. Li, Y. Li, H. Li, L. Zhang, J. Zhai, Y. Song, B. Liu, L. Jiang, and D. Zhu, "Super-hydrophobic surfaces: from natural to artificial," *Advanced materials*, vol. 14, no. 24, pp. 1857–1860, 2002.

[27] J. Long, P. Fan, D. Gong, D. Jiang, H. Zhang, L. Li, and M. Zhong, "Superhydrophobic surfaces fabricated by femtosecond laser with tunable water adhesion: from lotus leaf to rose petal," *ACS applied materials & interfaces*, vol. 7, no. 18, pp. 9858–9865, 2015.

[28] X. Tian, T. Verho, and R. H. Ras, "Moving superhydrophobic surfaces toward real-world applications," *Science*, vol. 352, no. 6282, pp. 142–143, 2016.

[29] J. Drelich, E. Chibowski, D. D. Meng, and K. Terpilowski, “Hydrophilic and superhydrophilic surfaces and materials,” *Soft Matter*, vol. 7, no. 21, pp. 9804–9828, 2011.

[30] L. Zhang, N. Zhao, and J. Xu, “Fabrication and application of superhydrophilic surfaces: a review,” *Journal of Adhesion Science and Technology*, vol. 28, no. 8-9, pp. 769–790, 2014.

[31] T. Otitoju, A. Ahmad, and B. Ooi, “Superhydrophilic (superwetting) surfaces: A review on fabrication and application,” *Journal of industrial and engineering chemistry*, vol. 47, pp. 19–40, 2017.

[32] A. Al Hossain, M. Yang, A. Checco, G. Doerk, and C. E. Colosqui, “Large-area nanostructured surfaces with tunable zeta potentials,” *Applied Materials Today*, vol. 19, p. 100553, 2020.

[33] M. Kobayashi, Y. Terayama, H. Yamaguchi, M. Terada, D. Murakami, K. Ishihara, and A. Takahara, “Wettability and antifouling behavior on the surfaces of superhydrophilic polymer brushes,” *Langmuir*, vol. 28, no. 18, pp. 7212–7222, 2012.

[34] S. Hoshian, V. Jokinen, V. Somerkivi, A. R. Lokanathan, and S. Franssila, “Robust superhydrophobic silicon without a low surface-energy hydrophobic coating,” *ACS applied materials & interfaces*, vol. 7, no. 1, pp. 941–949, 2015.

[35] A. K. Kota, Y. Li, J. M. Mabry, and A. Tuteja, “Hierarchically structured superoleophobic surfaces with ultralow contact angle hysteresis,” *Adv.Mater.*, vol. 24, no. 43, pp. 5838–5843, 2012.

[36] G. Zhang, X. Zhang, M. Li, and Z. Su, “A surface with superoleophilic-to-superoleophobic wettability gradient,” *ACS Appl. Mater. Interfaces*, vol. 6, no. 3, pp. 1729–1733, 2014.

[37] J. Yong, F. Chen, Q. Yang, Z. Jiang, and X. Hou, “A review of femtosecond-laser-induced underwater superoleophobic surfaces,” *Adv. Mater. Interfaces*, vol. 5, no. 7, p. 1701370, 2018.

[38] U. Baruah, A. Das, and U. Manna, “Synthesis of dual-functional and robust underwater superoleophobic interfaces,” *ACS Appl. Mater. Interfaces*, vol. 11, no. 31, pp. 28571–28581, 2019.

[39] T.-S. Wong, S. H. Kang, S. K. Tang, E. J. Smythe, B. D. Hatton, A. Grinthal, and J. Aizenberg, “Bioinspired self-repairing slippery surfaces with pressure-stable omniphobicity,” *Nature*, vol. 477, no. 7365, pp. 443–447, 2011.

[40] A. Lafuma and D. Quéré, “Slippery pre-suffused surfaces,” *EPL*, vol. 96, no. 5, p. 56001, 2011.

[41] B. R. Solomon, K. S. Khalil, and K. K. Varanasi, “Drag reduction using lubricant-impregnated surfaces in viscous laminar flow,” *Langmuir*, vol. 30, no. 36, pp. 10970–10976, 2014.

[42] S. Sett, X. Yan, G. Barac, L. W. Bolton, and N. Miljkovic, “Lubricant-infused surfaces for low-surface-tension fluids: promise versus reality,” *ACS Appl. Mater. Interfaces*, vol. 9, no. 41, pp. 36400–36408, 2017.

[43] D. J. Preston, Y. Song, Z. Lu, D. S. Antao, and E. N. Wang, “Design of lubricant infused surfaces,” *ACS Appl. Mater. Interfaces*, vol. 9, no. 48, pp. 42383–42392, 2017.

[44] M. Villegas, Y. Zhang, N. Abu Jarad, L. Soleymani, and T. F. Didar, “Liquid-infused surfaces: A review of theory, design, and applications,” *ACS Nano*, vol. 13, no. 8, pp. 8517–8536, 2019.

[45] S. Peppou-Chapman, J. K. Hong, A. Waterhouse, and C. Neto, “Life and death of liquid-infused surfaces: a review on the choice, analysis and fate of the infused liquid layer,” *Chem. Soc. Rev.*, 2020.

[46] J. Bico, U. Thiele, and D. Quéré, “Wetting of textured surfaces,” *Colloids Surf. A Physicochem. Eng. Asp.*, vol. 206, no. 1-3, pp. 41–46, 2002.

[47] J. S. Wexler, I. Jacobi, and H. A. Stone, “Shear-driven failure of liquid-infused surfaces,” *Physical review letters*, vol. 114, no. 16, p. 168301, 2015.

[48] I. Jacobi, J. Wexler, and H. A. Stone, “Overflow cascades in liquid-infused substrates,” *Phys. Fluids*, vol. 27, no. 8, p. 082101, 2015.

[49] A. Keiser, P. Baumli, D. Vollmer, and D. Quéré, “Universality of friction laws on liquid-infused materials,” *Phys. Rev. Fluid*, vol. 5, no. 1, p. 014005, 2020.

[50] J. S. Rowlinson and B. Widom, *Molecular theory of capillarity.* Courier Corporation, 2013.

[51] P.-G. De Gennes, F. Brochard-Wyart, and D. Quéré, *Capillarity and wetting phenomena: drops, bubbles, pearls, waves.* Springer Science & Business Media, 2013.

[52] B. Derby, “Inkjet printing of functional and structural materials: fluid property requirements, feature stability, and resolution,” *Annual Review of Materials Research*, vol. 40, pp. 395–414, 2010.

[53] E. W. Washburn, “The dynamics of capillary flow,” *Physical review*, vol. 17, no. 3, p. 273, 1921.

[54] S. Sanghavi, “Experimental and computational studies of capillary imbibition,” Master’s thesis, Stony brook university, 2016.

[55] A. Marmur, “The lotus effect: superhydrophobicity and metastability,” *Langmuir*, vol. 20, no. 9, pp. 3517–3519, 2004.

[56] M. Ma and R. M. Hill, “Superhydrophobic surfaces,” *Current opinion in colloid & interface science*, vol. 11, no. 4, pp. 193–202, 2006.

[57] J. Heverhagen, M. Tasinkevych, A. Rahman, C. T. Black, and A. Checco, “Slip length enhancement in nanofluidic flow using nanotextured superhydrophobic surfaces,” *Advanced Materials Interfaces*, vol. 3, no. 17, p. 1600303, 2016.

[58] A. M. Rahmani, A. Wang, V. N. Manoharan, and C. E. Colosqui, “Colloidal particle adsorption at liquid interfaces: capillary driven dynamics and thermally activated kinetics,” *Soft Matter*, vol. 12, no. 30, pp. 6365–6372, 2016.

[59] J. W. Gibbs, *The scientific papers of J. Willard Gibbs*, vol. 1. Longmans, Green and Company, 1906.

[60] F. Brochard-Wyart, J. M. Di Meglio, D. Quére, and P. G. De Gennes, “Spreading of nonvolatile liquids in a continuum picture,” *Langmuir*, vol. 7, no. 2, pp. 335–338, 1991.

[61] B. M. Jose and T. Cubaud, “Role of viscosity coefficients during spreading and coalescence of droplets in liquids,” *Physical Review Fluids*, vol. 2, no. 11, p. 111601, 2017.

[62] T. Blake and J. Haynes, “Kinetics of liquidliquid displacement,” *Journal of colloid and interface science*, vol. 30, no. 3, pp. 421–423, 1969.

[63] A. Siria, P. Poncharal, A.-L. Biance, R. Fulcrand, X. Blase, S. T. Purcell, and L. Bocquet, “Giant osmotic energy conversion measured in a single transmembrane boron nitride nanotube,” *Nature*, vol. 494, no. 7438, pp. 455–458, 2013.

[64] A. Duparré, M. Flemming, J. Steinert, and K. Reihs, “Optical coatings with enhanced roughness for ultrahydrophobic, low-scatter applications,” *Applied Optics*, vol. 41, no. 16, pp. 3294–3298, 2002.

[65] U. Manna and D. M. Lynn, “Fabrication of liquid-infused surfaces using reactive polymer multilayers: principles for manipulating the behaviors and mobilities of aqueous fluids on slippery liquid interfaces,” *Advanced Materials*, vol. 27, no. 19, pp. 3007–3012, 2015.

[66] R. Seemann, M. Brinkmann, E. J. Kramer, F. F. Lange, and R. Lipowsky, “Wetting morphologies at microstructured surfaces,” *Proceedings of the National Academy of Sciences*, vol. 102, no. 6, pp. 1848–1852, 2005.

[67] A. Tuteja, W. Choi, J. M. Mabry, G. H. McKinley, and R. E. Cohen, “Robust omniphobic surfaces,” *Proceedings of the National Academy of Sciences*, vol. 105, no. 47, pp. 18200–18205, 2008.

[68] L. Lurio, D. Lumma, A. Sandy, M. Borthwick, P. Falus, S. Mochrie, J. Pelletier, M. Sutton, L. Regan, A. Malik, *et al.*, “Absence of scaling for the intermediate scattering function of a hard-sphere suspension: Static and dynamic x-ray scattering

from concentrated polystyrene latex spheres," *Physical review letters*, vol. 84, no. 4, p. 785, 2000.

[69] S. Mochrie, A. Mayes, A. Sandy, M. Sutton, S. Brauer, G. Stephenson, D. Abernathy, and G. Grübel, "Dynamics of block copolymer micelles revealed by x-ray intensity fluctuation spectroscopy," *Physical review letters*, vol. 78, no. 7, p. 1275, 1997.

[70] D. Lumma, M. A. Borthwick, P. Falus, L. B. Lurio, and S. G. Mochrie, "Equilibrium dynamics in the nondiffusive regime of an entangled polymer blend," *Physical Review Letters*, vol. 86, no. 10, p. 2042, 2001.

[71] F. Mechanics, "White, frank m," 1998.

[72] D. Nandyala, Z. Wang, D. Hwang, T. Cubaud, and C. E. Colosqui, "Design, fabrication, and analysis of a capillary diode for potential application in water–oil separation," *ACS Applied Materials & Interfaces*, vol. 12, no. 41, pp. 45950–45960, 2020.

[73] T. Y. Choi, D. J. Hwang, and C. P. Grigoropoulos, "Femtosecond laser induced ablation of crystalline silicon upon double beam irradiation," *Applied surface science*, vol. 197, pp. 720–725, 2002.

[74] D. J. Hwang, C. P. Grigoropoulos, and T. Y. Choi, "Efficiency of silicon micromachining by femtosecond laser pulses in ambient air," *Journal of applied physics*, vol. 99, no. 8, p. 083101, 2006.

[75] D. J. Hwang, M. Kim, K. Hiromatsu, H. Jeon, and C. P. Grigoropoulos, "Three-dimensional opto-fluidic devices fabricated by ultrashort laser pulses for high throughput single cell detection and processing," *Applied Physics A*, vol. 96, no. 2, pp. 385–390, 2009.

[76] M. D. Abràmoff, P. J. Magalhães, and S. J. Ram, "Image processing with imagej," *Biophotonics international*, vol. 11, no. 7, pp. 36–42, 2004.

[77] B. Zhmud, F. Tiberg, and K. Hallstensson, "Dynamics of capillary rise," *Journal of colloid and interface science*, vol. 228, no. 2, pp. 263–269, 2000.

[78] N. Fries and M. Dreyer, "An analytic solution of capillary rise restrained by gravity," *Journal of colloid and interface science*, vol. 320, no. 1, pp. 259–263, 2008.

[79] Z. Wang, D. Nandyala, C. E. Colosqui, T. Cubaud, and D. J. Hwang, "Glass surface micromachining with simultaneous nanomaterial deposition by picosecond laser for wettability control," *Applied Surface Science*, vol. 546, p. 149050, 2021.

[80] A. Agarwal and J. Lang, *Foundations of analog and digital electronic circuits*. Elsevier, 2005.

[81] D. Leenaerts and W. M. Van Bokhoven, *Piecewise linear modeling and analysis*. Springer Science & Business Media, 2013.